

EXAMINING ULTRASONIC SCATTERING MECHANISMS IN FATTY LIVER  
PARENCHYMA VIA HISTOPATHOLOGICAL LIVER IMAGE

BY

YASHUO WU

THESIS

Submitted in partial fulfillment of the requirements  
for the degree of Master of Science in Electrical and Computer Engineering  
in the Graduate College of the  
University of Illinois Urbana-Champaign, 2021

Urbana, Illinois

Adviser:

Research Assistant Professor Aiguo Han

## Abstract

Quantitative ultrasound (QUS) techniques are diagnostically useful in assessing nonalcoholic fatty liver disease (NAFLD). From previous studies, the backscatter coefficient (BSC) correlates with liver fat fraction, but the mechanisms of the correlation have not been fully determined. Understanding the ultrasound scattering mechanisms will lead to better acoustic scattering models and potentially more accurate diagnostics. Several scattering mechanisms have been hypothesized and the following mechanism is tested in this thesis: Fat droplet deposition in hepatocytes alters the locations of hepatocyte nuclei, changing the spatial distribution of the nuclei, which leads to the change in the structure function, a factor of the BSC. The structure function, determined by the spatial distribution of the nuclei, is thus correlated with the fat fraction. Digitized histopathological liver slides were analyzed to test this hypothesis. Seventy-six (76) hematoxylin and eosin-stained liver histopathological slides from 46 participants with NAFLD and 10 participants without NAFLD were digitized at 40 $\times$  objective magnification. One to five regions of interest (ROIs) (453.6  $\mu\text{m} \times 453.6 \mu\text{m}$ ) were selected from each participant's slide(s), yielding 258 ROIs in total. For each ROI, hepatocyte nuclei and fat droplets were automatically recognized using two independent methods: the morphological processing method and the U-Net method. Fat droplets were also automatically recognized for each ROI. In addition, hepatocyte nuclei were manually annotated for a subset of ROIs ( $N = 47$ ). The structure function curves were calculated from the nuclear distributions obtained from the automatic and manual recognition methods. The liver fat fraction was determined from histology for each ROI by calculating the fractional surface area of fat droplets. Structure function was positively correlated with the liver fat fraction (Pearson's  $r \sim 0.45$ ,  $p < 10^{-4}$ ) below 25 MHz (including

clinically relevant frequencies 3 - 5 MHz) using the morphological processing method for nucleus recognition. Pearson's r value between the structure function and the fat fraction was approximately 0.40 ( $p < 10^{-4}$ ) below 20 MHz using the U-Net method for nucleus recognition. Structure function calculated from manually annotated nucleus positions had a positive correlation (Pearson's r ~ 0.45,  $p < 0.01$ ) with fat fraction below 25 MHz. In conclusion, this study shows the fat droplets change the distribution of hepatocyte nuclei, which is a factor contributing to the correlation between fat fraction and BSC.

## Acknowledgments

This thesis is made possible through the help and support from many people. I would like to thank my adviser, Professor Aiguo Han, for giving me the opportunity to do research and providing me with advice, expertise, and encouragement throughout this research. His hard work, vision, and motivation have inspired me deeply. He has trained me from the beginning and taught me to carry out and present the research clearly. It was a great privilege to work and study under his guidance. I must also thank Professor William D. O'Brien, Jr., Dr. Quang Tran, Dr. Rita Miller, and the rest of the Bioacoustics Research Laboratory for their research suggestions and advice. I am thankful for Professors Michael Andre, Mark Valasek, and Matthew Wallig who provided me data and guidance on histopathology.

I would like to thank my parents for their love and support for educating and preparing me for my future studies.

## Table of Contents

<b>Chapter 1: INTRODUCTION .....</b>	<b>1</b>
<b>1.1 Quantitative Ultrasound .....</b>	<b>1</b>
<b>1.2 QUS in NAFLD .....</b>	<b>2</b>
<b>1.3 Scattering Mechanisms .....</b>	<b>3</b>
<b>1.4 Structure Function .....</b>	<b>4</b>
<b>1.5 Purpose.....</b>	<b>5</b>
<b>Chapter 2: STRUCTURE FUNCTION THEORY .....</b>	<b>7</b>
<b>Chapter 3: METHODS.....</b>	<b>9</b>
<b>3.1 H&amp;E ROI Selection.....</b>	<b>9</b>
<b>3.3 Fat Fraction Determination .....</b>	<b>12</b>
<b>3.4 Automatic Nuclei Recognition.....</b>	<b>13</b>
<b>3.5 Manual Nuclei Recognition .....</b>	<b>27</b>
<b>3.6 Structure Function Calculation from ROI.....</b>	<b>28</b>
<b>3.7 Evaluation of Automatic Nucleus Recognition.....</b>	<b>29</b>
<b>3.8 Comparison of the Structure Function of ROIs with Different Fat Fractions.....</b>	<b>30</b>
<b>Chapter 4: RESULTS AND DISCUSSION .....</b>	<b>32</b>
<b>4.1 Fat Fraction Result .....</b>	<b>32</b>
<b>4.2 Automatic Nuclei Recognition Result .....</b>	<b>33</b>
<b>4.3 Structure Function Result.....</b>	<b>36</b>
<b>4.4 Correlation between Structure Function and Fat Fraction .....</b>	<b>38</b>
<b>4.6 Comparison of the Structure Function .....</b>	<b>48</b>
<b>4.7 Special NAFLD Cases .....</b>	<b>51</b>
<b>4.8 Discussion.....</b>	<b>52</b>
<b>Chapter 5: CONCLUSION AND FUTURE WORK.....</b>	<b>54</b>
<b>5.1 Conclusion.....</b>	<b>54</b>
<b>5.2 Future Work .....</b>	<b>54</b>

<b>REFERENCES .....</b>	<b>56</b>
-------------------------	-----------

# Chapter 1: INTRODUCTION

## 1.1 Quantitative Ultrasound

Quantitative ultrasound (QUS) techniques have promising clinical applications in tissue characterization and disease diagnosis [1]. QUS techniques can provide specific numbers to characterize ultrasound signals and analyze the signals to extract underlying tissue microstructure information. QUS imaging is different from conventional B-mode imaging in the following aspects. Conventional B-mode imaging utilizes envelopes of backscattered radiofrequency (RF) signals to display tissue structures qualitatively. The phase information of RF data is not used in conventional B-mode imaging. This limitation of B-mode imaging leads to inaccuracy of diagnostic ultrasound [1]. QUS imaging takes advantage of the raw RF data and can yield system- and operator-independent parameters containing quantitative tissue microstructure information that cannot be acquired from conventional B-mode imaging. QUS techniques improve diagnostic sensitivity and specificity by providing quantitative estimates of tissue properties such as scatterer shape, size, number density, and acoustic impedance contrast. QUS was utilized for tissue characterization for various organs [2]. For example, QUS methods have been used in the eye [3], heart [4], prostate [5], kidney [6], and breast [7]. Also, QUS has proposed monitoring cell death [8] and diagnose diseases [9]. Among other successes, recent human studies have demonstrated the capabilities of QUS techniques in quantifying liver steatosis [10] – [12].

QUS techniques yield two fundamental parameters from raw RF data, attenuation coefficient (AC) and backscatter coefficient (BSC). AC measures the loss of ultrasound energy in tissue and is defined as the rate of amplitude before and after the ultrasound signal traveling through tissue. BSC is a fundamental property of tissue that measures the fraction of ultrasound energy returned from tissue and is defined as the differential backscattering cross-section per unit volume at a scattering angle of 180 degrees. BSC is related to underlying tissue structure and is sensitive to the tissue microstructure [1].

## 1.2 QUS in NAFLD

Nonalcoholic fatty liver disease (NAFLD) is one of the most common liver diseases, affecting approximately 25% of the human population [13], [14], [15]. NAFLD is considered a serious health risk [16], affects both children and adults, and continues to affect more people every year [15]. The earliest characteristic histologic feature of NAFLD is hepatic steatosis, defined as the accumulation of fat droplets within hepatocytes. One-third of NAFLD cases develop into nonalcoholic steatohepatitis (NASH), which can progress to serious conditions and contribute to the development of fibrosis, cirrhosis, and even hepatocellular carcinoma [13], [14].

Laboratory tests for detecting and evaluating participants with suspected NAFLD include a serum panel of liver tests [17], [18]. However, these tests are not successful at diagnosing NAFLD [19]. Various imaging modalities have been explored for improving the NAFLD diagnosis [20] – [23]. Conventional ultrasonography is the most commonly used imaging modality to diagnose NAFLD. However, conventional ultrasonography is qualitative,

system and operator dependent, with modest accuracy in diagnosing liver steatosis. A better diagnosis approach is needed.

QUS has shown to be promising for detecting steatosis and quantify liver fat. Several QUS parameters, e.g., AC, BSC, Lizzi-Feleppa intercept, and midband [12] are correlated with liver fat content. In particular, the BSC has been shown to correlate with fat fraction in several human studies [12], [24], [25] – [27]. For example, in the study by Lin et al. [24], the BSC was estimated for participants with and without NAFLD and compared with magnetic resonance imaging proton density fat fraction (MRI-PDFF). A Spearman's rank correlation coefficient of 0.80 was reported between BSC and MRI-PDFF [24]. Another study [12] reported that BSC had a Pearson Correlation Coefficient of 0.58 with MRI-PDFF in a different cohort. Although the BSC was observed to positively correlate with the MRI-PDFF in previous studies, the mechanism of the positive correlation between BSC and MRI-PDFF has not been elucidated. Understanding the underneath mechanism may guide the proper use and further improvement of QUS techniques. This thesis investigates a scattering mechanism to explain the positive correlation between BSC and liver fat fraction.

### **1.3 Scattering Mechanisms**

Acoustic scattering contains two components: incoherent scattering and coherent scattering [2]. Incoherent scattering is determined by individual scatterer's intrinsic characteristics, such as the scatterer geometry and acoustic impedance [2]. Coherent scattering is caused by correlations among scatterers and is affected by scatterers' spatial distribution.

Incoherent scattering was studied extensively and was modeled by form factor models. Many models such as the spherical Gaussian model [28], fluid-filled sphere [29], spherical shell [30], and two concentric spheres [25] were proposed to model the incoherent scattering. In some cases, these models can achieve reasonable results. For example, the widely used spherical Gaussian model could model the soft tissue scattering properties [26], [27], [31]. However, the spherical Gaussian model cannot provide accurate tissue property estimates, suggesting more factors need to be included in the model. Papers [8], [32], [2], [33], [34] showed that, under the circumstances of the dense media, the correlation of scatterer positions has a significant contribution to the scattering. In dense media, coherent scattering caused by correlation among scatterer positions cannot be neglected. Also, the correlation of scatterer positions is nonnegligible for sparse media where the scatterers are arranged in a nonrandom pattern.

## 1.4 Structure Function

Scattering caused by the spatial correlation among scatterers can be modeled by the structure function, proportional to the squared modulus of the Fourier transform of the scatterers' positions. V. Twersky applied the structure function into the field of acoustic scattering in his papers ([35] and [36]). He described a theoretical structure function expressed as a function of the correlation length between scatterers. Fontaine et al. proposed to use structure function to model the spatial arrangement of red blood cells.

Structure function plays an important role in achieving accurate modeling of acoustic scattering. Han and O'Brien [2] indicated the structure function needs to be included in the modeling of scattering in dense media. Franceschini et al. [33] demonstrated that estimating BSC

by taking structure function into account can achieve better agreement between experiential data and models than without including structure function as a factor. In addition, in the field of ultrasonic characterization of blood, structure function was applied to address the difficulty of modeling aggregated cells [37],[38], [39].

Han and O'Brien [2] conducted experiments in cell pellet biophantoms and extracted the structure function from the BSC and verified the extracted structure function. Han et al. [40] later developed the structure function estimation algorithm using histological tissue sections, and the algorithm was applied to estimate structure function in this thesis.

This thesis studies the structure function in fatty livers. In fatty livers, the fat droplets were observed to push the nuclei and, as a result, change the nuclei spatial distribution. The change in nuclei spatial distribution could lead to changes in the structure function of the nuclei. If the hepatocyte nuclei were major scattering sites in the liver, the BSC from the liver would be affected accordingly.

## 1.5 Purpose

The purpose of this study is to investigate how liver fat droplets change the structure function of hepatocyte nuclei. Digitized hematoxylin and eosin (H&E)-stained histopathological liver slides are used in the study. The structure function of hepatocyte nuclei was estimated from histological slides of participants with NAFLD and participants without NAFLD. Analyzing the histological slides can improve the understanding of the relationships between BSC data and histology. A clear understanding of the mechanisms by which liver fat droplet deposition causes changes in

BSC will guide the proper use of the QUS techniques and lead to further improvement of the techniques.

We have hypothesized two independent mechanisms of acoustic scatterers in fatty liver. First, hepatocyte nuclei are acoustic scatterers and fat droplet deposition in hepatocytes alters the locations of the hepatocyte nuclei within the hepatocytes, which changes the spatial distribution of the nuclei. We verified that when the scatterer positions are dependent, the structure function must be added to the BSC model to account for the correlations between scatterer positions. We utilized the histological slides to study the real scatterers in the human liver. The second mechanism is that fat droplets constitute acoustic scatterers in the liver, which causes more scattering and increases BSC. This thesis only focuses on examining the first mechanism and the second mechanism is briefly discussed in Section 5.2.

## Chapter 2: STRUCTURE FUNCTION THEORY

The structure function theory is introduced as follows. Consider a plane wave incident on a scattering volume that contains  $N$  discrete scatterers. The differential scattering cross-section per unit volume,  $\sigma_d$ , observed in the far-field, can be expressed as [30], [40]

$$\sigma_d(\mathbf{K}) = \frac{1}{V} \left| \sum_{j=1}^N \Phi_j(\mathbf{K}) e^{i\mathbf{K} \cdot \mathbf{r}_j} \right|^2, \quad (1)$$

where  $\mathbf{r}_j$  is the position of the  $j$ th scatterer,  $\Phi_j(\mathbf{K})$  is the complex scattering amplitude of the  $j$ th scatterer and  $\mathbf{K}$  is the scattering vector, whose magnitude is given by  $|\mathbf{K}| = 2k\sin(\theta/2)$ , where  $\theta$  is the scattering angle, and  $k$  is the wavenumber. If the scatterers are spatially uncorrelated and  $N$  is large, the scattering is incoherent and the expected differential cross-section per unit volume becomes

$$\sigma_{d,incoherent} = \frac{1}{V} \sum_{j=1}^N |\Phi_j(\mathbf{K})|^2. \quad (2)$$

The structure function is defined as

$$S(\mathbf{K}) = \frac{\sigma_d(\mathbf{K})}{\sigma_{d,incoherent}(\mathbf{K})}. \quad (3)$$

Assuming the complex scattering amplitudes  $\Phi_j(\mathbf{K})$  are identical for all scatterers, (3) may be simplified as

$$S(\mathbf{K}) = \frac{1}{N} \left| \sum_{j=1}^N e^{-i\mathbf{K} \cdot \mathbf{r}_j} \right|^2. \quad (4)$$

Equation (4) describes that the structure function is determined by scatterers' spatial positions in 3D. Studies [25], [41], [42] validated that structure function can be estimated from 2D histological tissue sections instead of the 3D in isotropic scattering media. This thesis used the

2D version of equation 4 to calculate structure function from histological slides as described in Section 3.6.

## Chapter 3: METHODS

This chapter describes the methodologies to determine the fat fraction, recognize hepatocyte nuclei, and calculate structure function using digitized H&E liver histological slides. Sections 3.1 and 3.2 discuss H&E ROI selection and image pre-processing. The determination of fat fraction is described in Section 3.3. Section 3.4 introduces the methods that were developed to recognize hepatocyte nuclei automatically. Section 3.5 introduces how hepatocyte nuclei were recognized manually. Section 3.6 describes the calculation of structure function from recognized hepatocytes nuclei. Section 3.7 describes how the structure function results were evaluated.

### 3.1 H&E ROI Selection

Hematoxylin and eosin (H&E) slides were used to determine the nuclear position and fat fraction of fatty liver in this thesis. Hematoxylin is a basic dye used in combination with aluminum ions to stain acidic structures with a purplish-blue color [9], such as nuclei. Eosin is an acidic dye that stains the cytoplasm in pink. In H&E slides, fat droplets appear to be large, hollow, and unstained regions. H&E-stained histopathological slides provide an overview of tissue structure and show the distribution of hepatocyte nuclei [43].

This thesis uses H&E slides gathered by an experienced pathologist (Professor Mark A. Valasek) and a medical physicist (Professor Michael P. Andre) of the University of California, San Diego. Seventy-six (76) H&E-stained liver slides were digitized at 40 $\times$  apparent magnification using an Aperio AT2 scanner (Leica Biosystems, Germany).

A total of 258 ROIs were obtained from the histological slides of 56 participants. ROIs were analyzed instead of the whole slides because ROIs contain only human liver regions and exclude the blank area in the slides. ROIs were chosen randomly, avoiding artifacts such as tissue folds (causing a loss of detail in the folding part) and tearing artifacts (affecting nuclei spatial distribution). Each ROI had a size of  $453.6 \mu\text{m} \times 453.6 \mu\text{m}$  with a resolution of 3.97 pixels/ $\mu\text{m}$ , corresponding  $1800 \text{ pixels} \times 1800 \text{ pixels}$ . This ROI size was chosen to be as large as possible while avoiding blank regions on the slides;  $453.6 \mu\text{m}$  was slightly less than the width of the liver tissue strips on the slides. Five ROIs were attempted to be obtained from each slide. However, some slides were too small to cover five ROIs without the artifacts mentioned above. Therefore, one to five ROIs were eventually chosen per slide, depending on the liver tissue area and the presence of artifacts. All the slides used and ROIs picked in this thesis are shown in Table 1.

Scanner	Apparent Magnification	MPP (um/pixel)	Number of Slides	Number of ROIs with NAFLD
Leica AT2	40x	0.252	76	258

Table 1: H&E Slides and ROIs Used in the Thesis

Figure 1 is an example of ROI from the Leica AT2 scanner. MATLAB (The Mathworks Inc., Natick, MA) was used to read the histological slides and select ROIs with the following steps. First, a rectangular region with a typical size of  $882 \times 882 \mu\text{m}$  ( $3200 \times 3200$  pixels) was drawn on the slide to cover a part of the histological section large enough to contain an ROI in Figure 1 (a). Second, the slides were rotated, if necessary, such that the sides of the tissue strips would appear horizontal or vertical on the computer screen as shown in Figure 1 (b). After the

rotation, a  $453.6 \mu\text{m} \times 453.6 \mu\text{m}$  square ROI was placed inside the large rectangular region, avoiding blank space and artifacts.

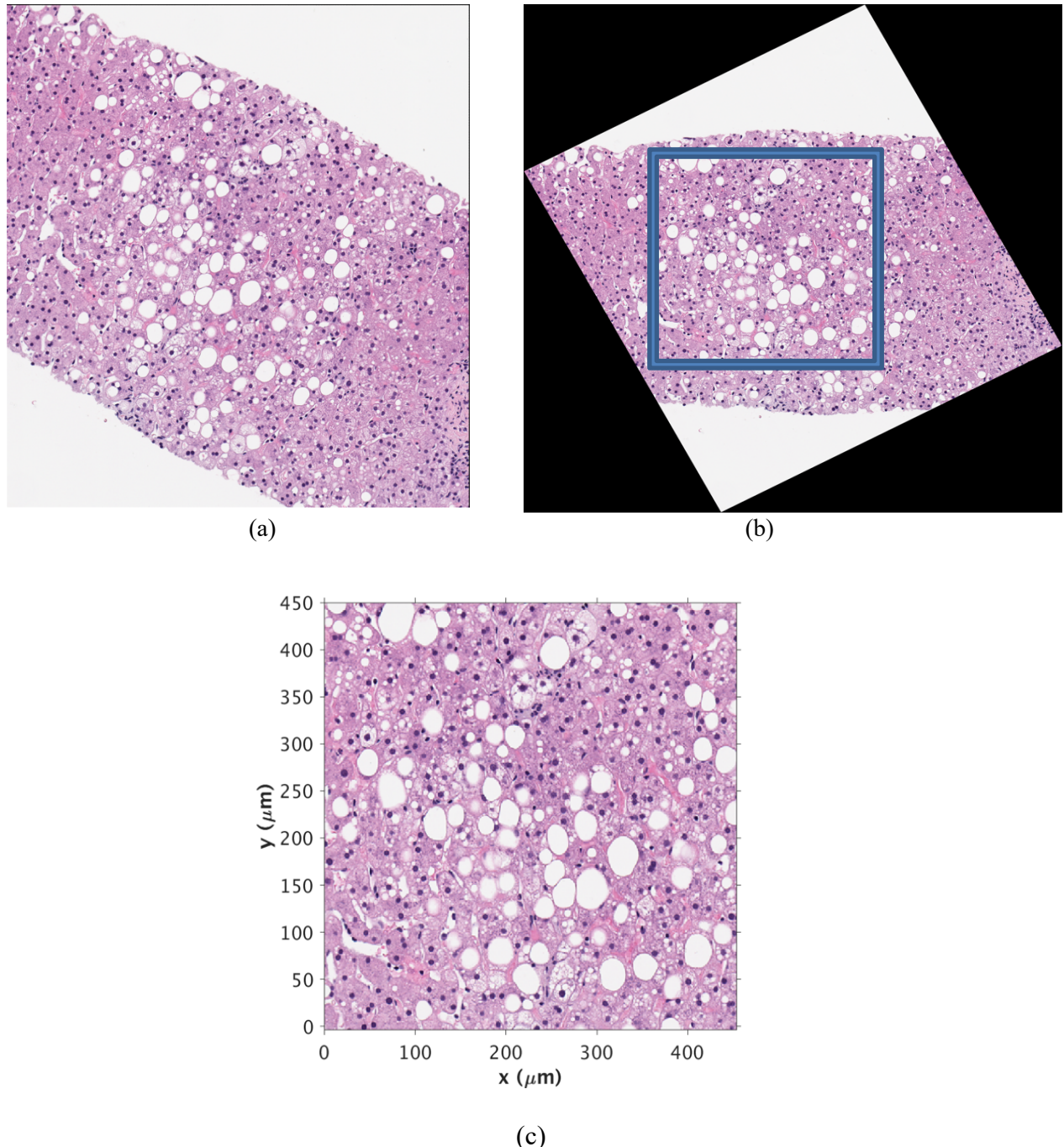


Figure 1: (a) An example rectangular region that was chosen from a histological section. (b) An example result after rotation of (a). (c) An example ROI is chosen from (b) before stain normalization.

### 3.2 Image Pre-Processing

A stain normalization algorithm [44] was applied to the ROIs (Figure 2) as an image pre-processing step to remove the stain variation among different histological samples and regions.

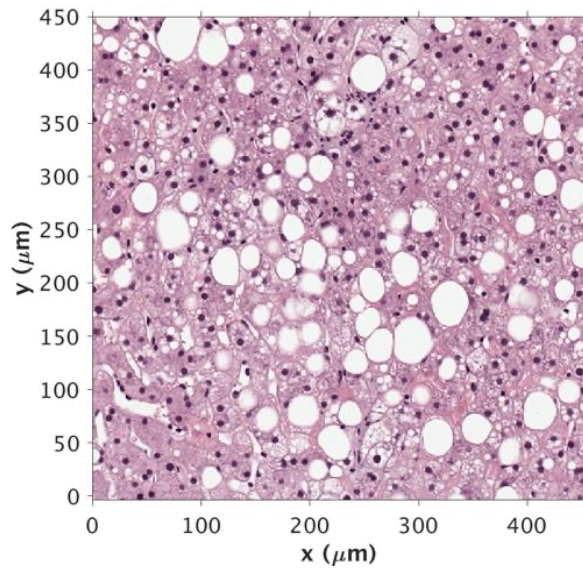


Figure 2: Stain-normalized version of Figure 1 (c).

### 3.3 Fat Fraction Determination

#### 3.3.1 Fat Droplets Recognition

Fat droplets were recognized automatically to calculate the fat fraction for each ROI. Fat droplets were recognized based on color, shape, and size. In terms of color, fat droplets appeared white in all ROIs. A binary mask of the same size as the original ROI was created when three color

channels (red, green, and blue) all had channel intensity values ranged from 200 to 255. In terms of shape, fat droplets were generally round. On the resulting mask, a circularity threshold was applied to all the recognized objects. The threshold was manually adjusted for each ROI. The resulting circularity threshold varied from 0.25 to 1.2. In terms of the size, most fat droplets had a radius larger than 3  $\mu\text{m}$  (10 pixels), and a 3  $\mu\text{m}$  threshold was applied. The above fat droplet recognition algorithm was implemented in Python 3.7.0.

### 3.3.2 Fat Fraction in ROIs and Participants

The fat fraction was determined on the per-ROI level and per-participant level. The per-ROI level fat fraction was determined histologically for each ROI by calculating the fraction of the ROI area occupied by fat droplets. Each ROI yielded a histologically determined fat fraction value.

The per-participant fat fraction was determined by the MRI proton density fat fraction [45]. MRI-PDFF was used as a reference of the fat fraction of a participant by comparing it with the average of the fat fraction obtained from ROIs of the same participant. The MRI technique individually measured the PDFF for each of the 8 Couinaud segments of the liver. The average of segments 5-8 (right lobe) was used to represent the MRI-PDFF in each participant. The right lobe was used because our histology slides were acquired from the right lobe.

## 3.4 Automatic Nuclei Recognition

Strategies were developed to automatically recognize hepatocyte nuclei from H&E-stained histological slides. Section 3.4.1 describes the morphological image processing method to recognize hepatocyte nuclei and lymphocytes. Sections 3.4.2 – 3.4.5 aim to classify the hepatocyte versus lymphocyte nuclei because the hepatocyte nuclei, rather than lymphocyte nuclei, were assumed to be the primary scattering sites in this thesis. Section 3.4.6 shows special cases that may negatively affect the accuracy of automatic recognition developed in the morphological processing method. Section 3.4.7 provides an alternative approach to automatic nuclei recognition.

### **3.4.1 Morphological Image Processing Method**

A series of operations were developed to automatically recognize hepatocyte nuclei. First, the k-means ( $k = 4$ ) clustering technique was used to classify the pixels based on colors into four categories: white, light pink, pink, and blue. The blue of hematoxylin was mostly received by the nuclei, while the remaining background (e.g., cytoplasm) received more light pink and pink from eosin. A binary image consisting of the nuclei and the background was then generated (e.g., Figure 3a).

A series of morphological operations were applied to the resulting binary images (Figure 3a) to improve the nuclei recognition results. The morphological opening was applied to remove objects much smaller than typical hepatocyte nuclei (e.g., Figure 3b), and the closing operation was used to fill in holes inside the nuclei (e.g., Figure 3c). The structuring element for opening and closing was 20 and 8 pixels, respectively. After that, objects with an eccentricity greater than 0.95 were removed (e.g., Figure 3d). Then, an opening operation was applied once more to

remove objects of radii less than 30 pixels (e.g., Figure 3e), followed by a closing operation to fill holes of radii less than 4 pixels (e.g., Figure 3f). Afterward, a flood fill algorithm was performed to fill in all holes (e.g., Figure 3g), followed by the third opening operation (structuring element = 20 pixels) (e.g., Figure 3h). Finally, the watershed method [46] was applied to separate connected objects (e.g., Figure 3i). After these steps, lymphocyte nuclei were misrecognized as hepatocyte nuclei. Further steps were developed to separate these two types of nuclei as described in Section 3.4.2.

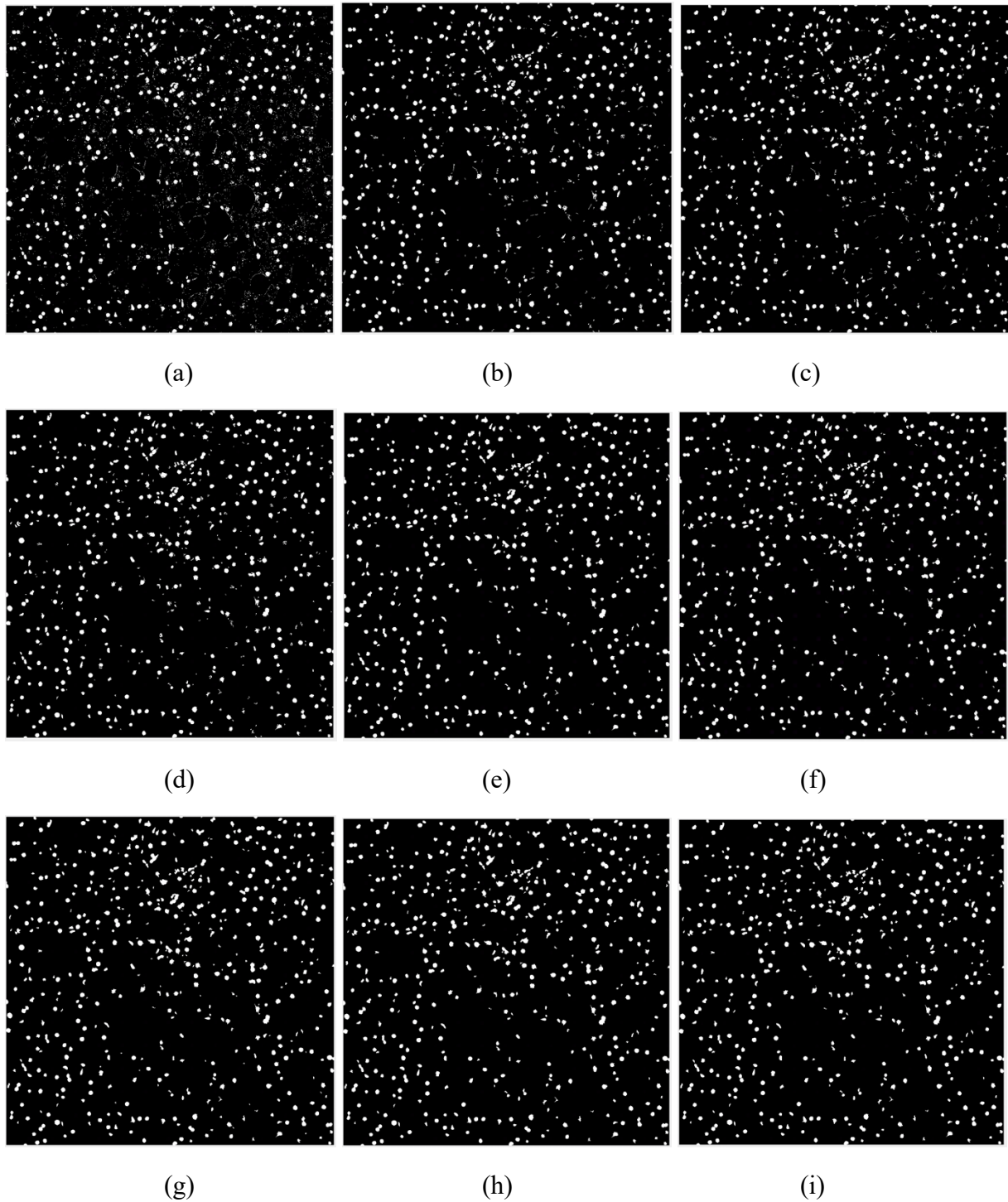
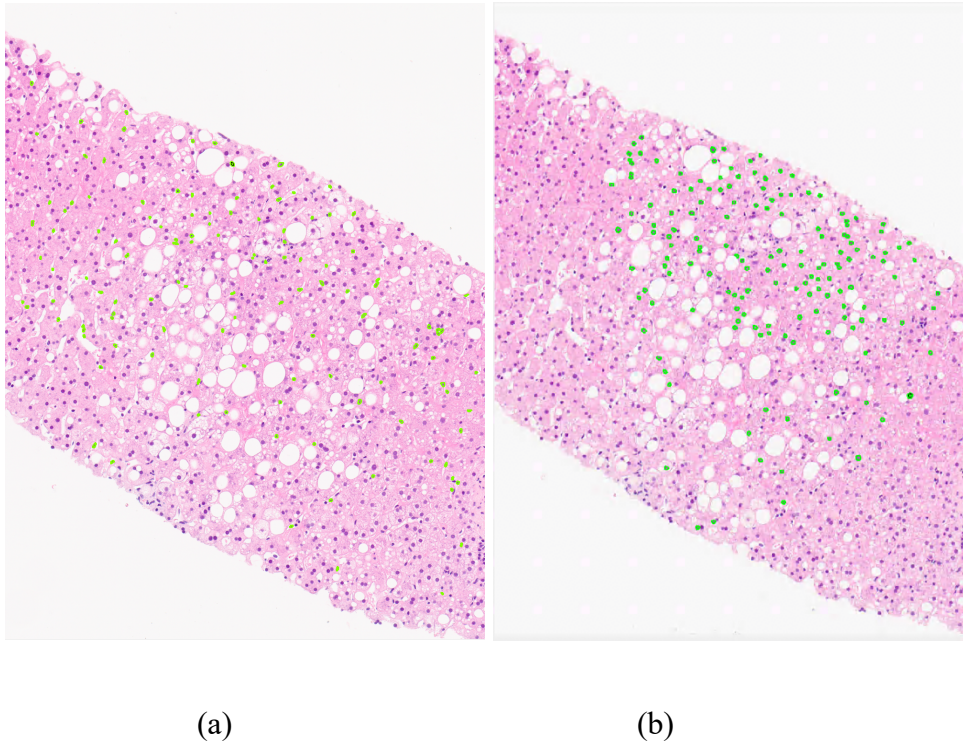


Figure 3: Binary images ( $453 \mu\text{m} \times 453 \mu\text{m}$ ) representing the intermediate results after (a) K-means pixel classification, (b) first morphological opening, (c) first morphological closing, (d) object filtering based on eccentricity, (e) second morphological opening, (f) second morphological closing, (g) flood fill, (h) third morphological opening, and (i) watershed operations.

### **3.4.2 Classification of Lymphocyte nuclei versus Hepatocyte Nuclei**

This thesis explores how the fat droplets change hepatocyte nuclei distribution. However, the morphological processing steps described in section 3.4.1 recognized both hepatocyte nuclei and lymphocyte nuclei. An algorithm was developed to classify the two types of nuclei. The color and texture differences between the two types of nuclei were explored to develop the classification algorithm. To explore the difference, a dataset was constructed by manually segmenting both types of nuclei. Histological section from each participant was enlarged to  $200\times$  on a 25" monitor such that each pixel occupied  $5\times 5$  screen pixels for clear visibility during manual segmentation. Aperio ImageScope was used to annotate the boundary of nuclei with a laser mouse and output an XML file containing boundaries for all the recognized nuclei in the ROI. Figures 4 (a) and (b) show examples of the manual segmentation results for hepatocyte nuclei and lymphocyte nuclei, respectively.



(a)

(b)

Figure 4: (a) Boundary of manually segmented lymphocyte nuclei in green. (b) The boundary of manually segmented hepatocyte nuclei in green.

### 3.4.3 Color Analysis

In a histological section (e.g., Figure 4), the mean and variance of each color channel (red [R], green [G], and blue [B], 8 bits, ranging from 0 to 255) were calculated from the pixel values of each manually segmented nucleus (lymphocyte nucleus or hepatocyte nucleus). The color channel histograms were plotted (Figures 5–8). The staining colors for lymphocyte and hepatocyte nuclei were different because of the differences in molecular components. Comparing the staining colors between lymphocyte and hepatocyte nuclei provides information on separating lymphocyte and hepatocyte nuclei.

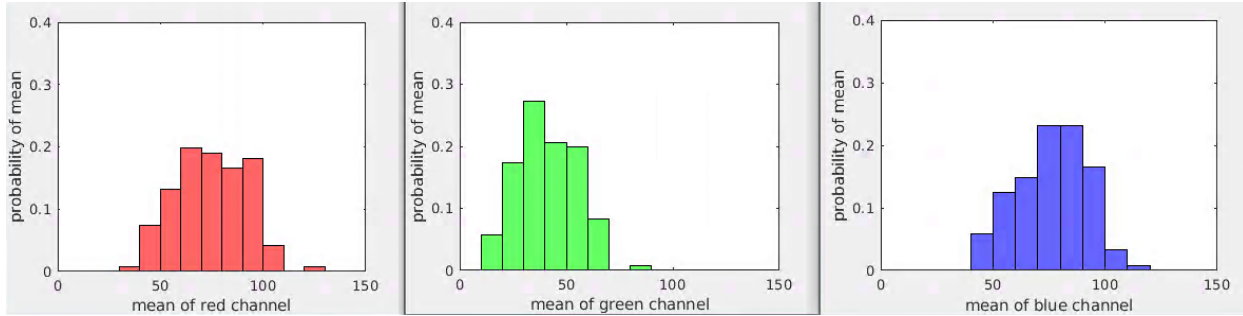


Figure 5: Example normalized histograms for the mean of the R, G, B channel values for lymphocyte nuclei in Figure 4 Bin width = 10.

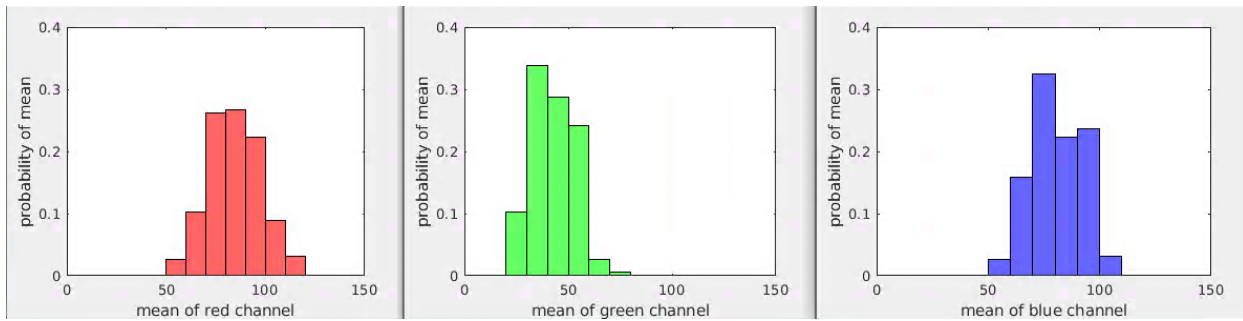


Figure 6: Example normalized histograms for the mean of the R, G, B channel values for hepatocyte nuclei in Figure 4. Bin width = 10.

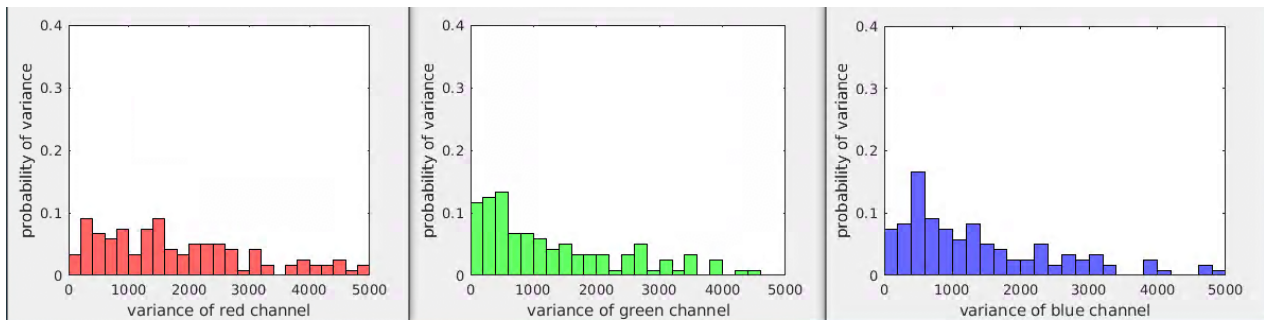


Figure 7: Example normalized histograms for the variance R, G, B channel values for lymphocyte nuclei in Figure 4. Bin width = 250.

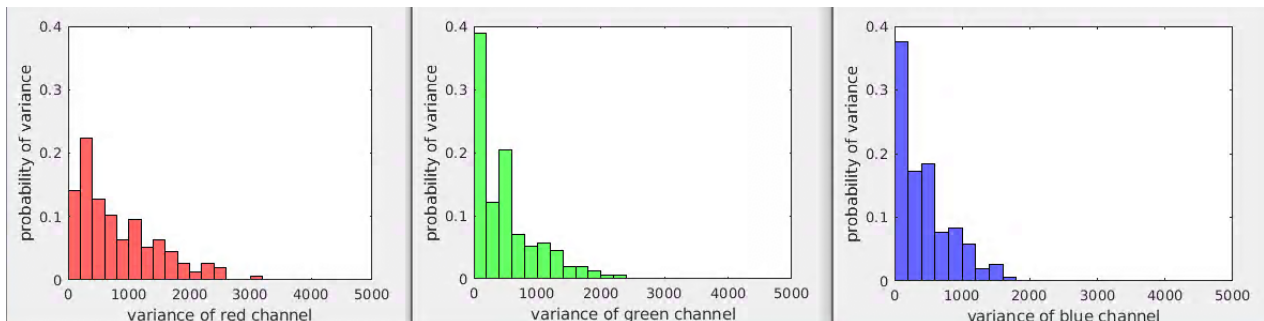


Figure 8: Example normalized histograms for variance R, G, B channel values for hepatocyte nuclei in Figure 4. Bin width = 250.

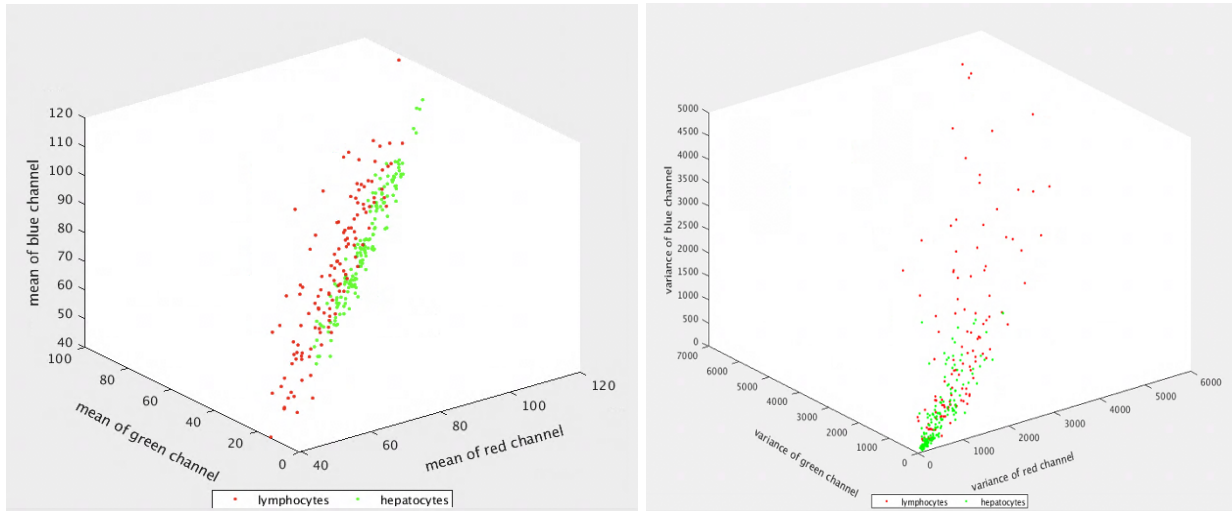


Figure 9: (a) 3-D scatter plot of the mean of R, G, B channels for each lymphocyte nucleus (red dots) and each hepatocyte nucleus (green dots). (b) 3-D scatter plot of the variance of R, G, B channels for each lymphocyte (red dots) and each hepatocyte (green dots).

There is no clear visual indication from Figures 5 – 8 that the color information from individual channels could classify lymphocyte nuclei versus hepatocyte nuclei. However, combining the information from all three color channels showed better separation between the two types of nuclei (e.g., Figure 9).

To better utilize the color information, the mean and variance of R, G, B channels from the pixel values in manually segmented lymphocyte nuclei and hepatocyte nuclei were also calculated on an optical density (OD) scale [44]. The transformation relationship between the OD and the intensity is

$$OD = -\log_{10}(I), \quad (5)$$

where  $I$  equals array [R, G, B] and R, G, B was each normalized to [0, 1] in OD scale.

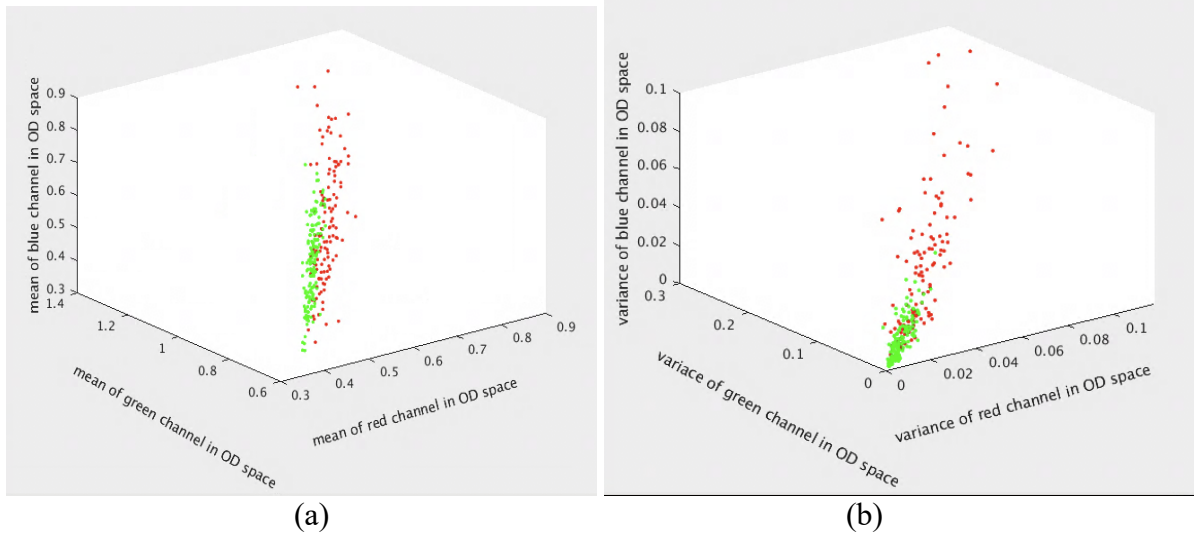


Figure 10: (a) Mean of lymphocyte (red) and hepatocyte (green) nuclei in OD space. (b) The variance of lymphocyte (red) and hepatocyte (green) nuclei in OD space.

Figures 9 and 10 support that the color information showed the potential to separate hepatocyte and lymphocyte nuclei, thereby justifying the use of color information when developing the separation method.

### 3.4.4 Texture Analysis

In addition to the color information, texture information was used to classify hepatocyte and lymphocyte nuclei. Texture features provided information on the spatial arrangement of colors and intensities in a nucleus. The gray-level co-occurrence matrix (GLCM, [47]) method was applied to calculate texture features. GLCM describes the inter-relationship between one pixel and its neighbors and yields numerical structures associated with the texture pattern of an image. The following texture parameters, contrast, energy, entropy, correlation, and homogeneity, were calculated from GLCM for each recognized object. For all the recognized lymphocyte and

hepatocyte nuclei, a squared mask ( $40 \times 40$  pixels) was placed on each recognized object (Figure 11). We chose the size of the squared mask because  $40 \times 40$  pixels could cover the largest nucleus and all nuclei could occupy the majority of the  $40 \times 40$  pixels square. Other than the recognized pixel squares, the remaining pixels were assigned to zero in the selected histological section (e.g., Figures 11 (a), (b)). Statistical measures were extracted where each square corresponds to a GLCM after changing the colored figures to grayscale by Matlab command ‘rgb2gray’ in Figure 12. The GLECM was constructed for each  $40 \times 40$  pixel square. The GLCM of the square is expressed as  $p$ , and  $(i, j)$  is the coordinate in the square. GLCM was calculated based on horizontal proximity of the pixels: [0, 1].

Among the five texture parameters, contrast measures the local variations in GLCM. A higher contrast value corresponds to more variation in an image. In other words, contrast reflects on the range of color distribution. The color of lymphocyte nuclei is distributed more evenly than the hepatocyte nuclei by observation. Therefore, the contrast parameter was explored to separate lymphocyte and hepatocyte nuclei. Contrast was calculated from:

$$\text{Contrast} = \sum_{i,j} |i - j|^2 p(i,j).$$

Correlation measures the joint probability occurrence of the specified pixel pairs. A higher correlation value indicates a larger amount of linear structure. The formula may be expressed as

$$\text{Correlation} = \sum_{i,j} \frac{(i-\mu_i)(j-\mu_j)p(i,j)}{\sigma_i \sigma_j}.$$

Energy, a measure of textural uniformity of an image, provides the sum of squared elements in the GLCM. Energy is from 0 to 1. Energy is 1 for a constant image. Energy was computed as follows:

$$\text{Energy} = \sum_{i,j} p(i,j)^2.$$

Entropy is a measure of the randomness of the intensity distribution. Entropy is highest when all entries in GLCM are of similar magnitude and the lowest when each individual entry in GLCM is unique. The formula may be expressed as

$$\text{Entropy} = \sum_{i,j} p(i,j) \log_2(p(i,j)).$$

Homogeneity measures the closeness of the distribution of elements in the GLCM to the GLCM diagonal. If an image tends to be clustered around the main diagonal, the homogeneity will result in a small value. Homogeneity achieves its largest value when most of the occurrences in GLCM are concentrated near the main diagonal. Homogeneity is defined as:

$$\text{Homogeneity} = \sum_{i,j} \frac{p(i,j)}{1+|i-j|}.$$

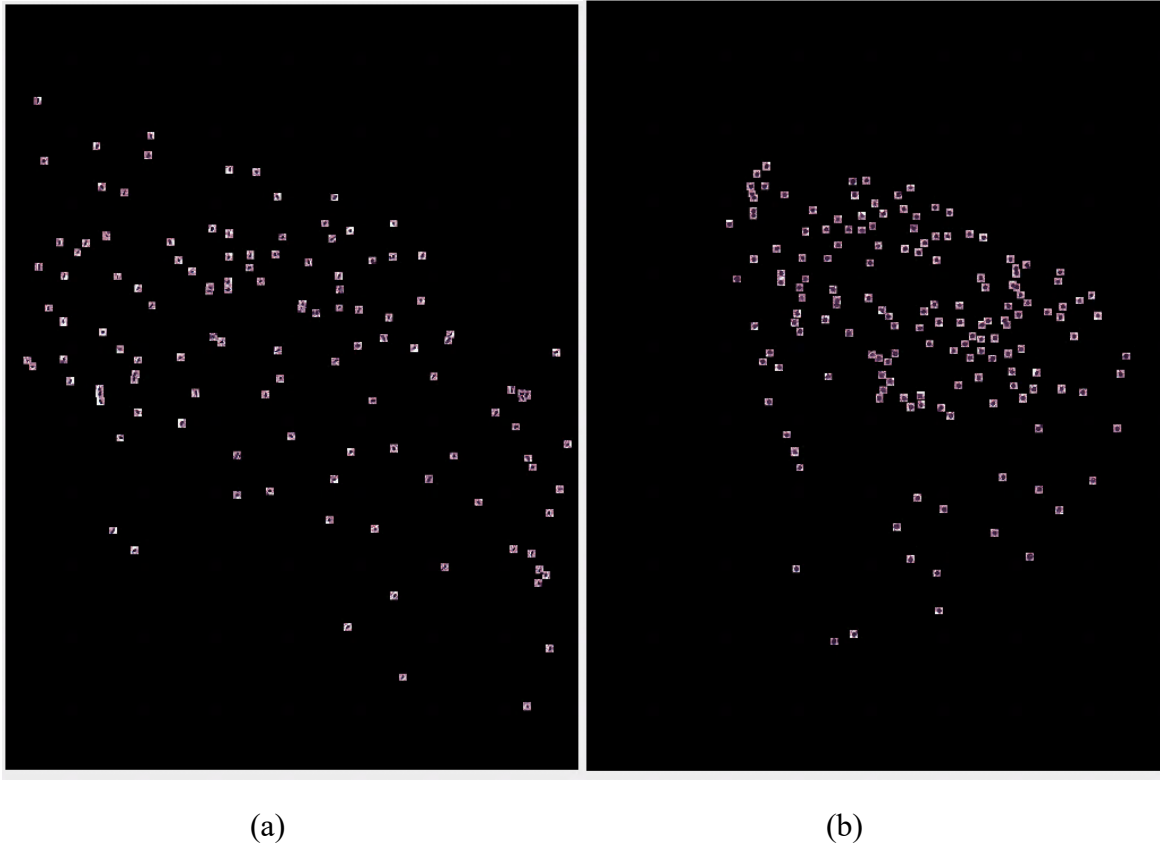


Figure 11: (a) Squared mask for lymphocyte nuclei. (b) Squared mask for hepatocyte nuclei.

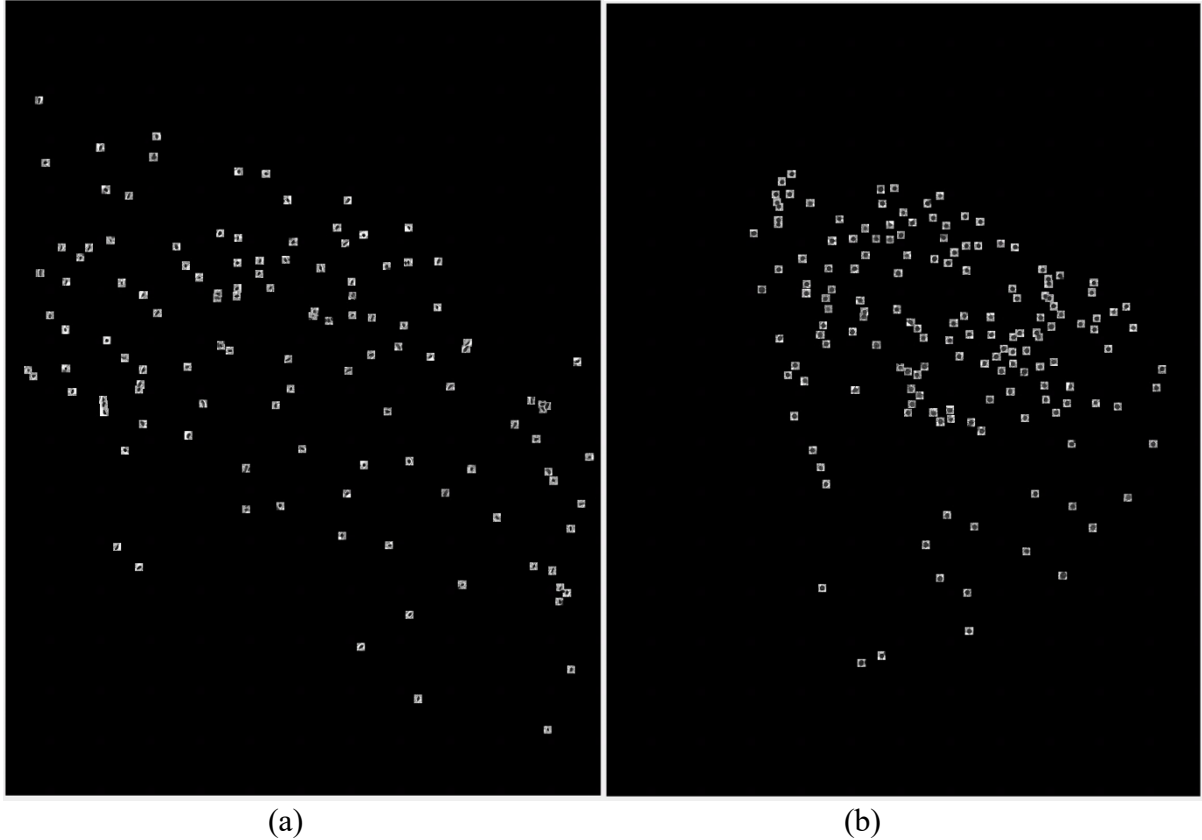


Figure 12: (a) Squared mask for lymphocyte nuclei in grayscale. (b) Squared mask for hepatocyte nuclei in grayscale.

### 3.4.5 Classifier for Lymphocyte and Hepatocyte Nuclei

A linear discriminant analysis classifier was constructed to distinguish the lymphocyte nuclei from hepatocyte nuclei, based on all 17 parameters (contrast, correlation, energy, entropy, homogeneity, mean and variance of RGB, and mean and variance of RGB in OD space) described in Sections 3.4.3 and 3.4.4.

To construct a linear discriminant analysis classifier, we analyzed 11 histological sections from 11 participants. The nuclei were manually segmented from these 11 histological sections. The dataset was divided into a training set (6 sections) and a test set (5 sections). A 6-fold cross-

validation was performed within the training set to select the best feature combination ( $\leq 3$  features). The test set provided an unbiased evaluation of the trained classifier.

Three features, red mean, red variance in OD scale, and energy, were used in the final linear discriminant analysis classifier. The classifier achieved a 95% accuracy in classifying between hepatocyte nuclei and lymphocyte nuclei in the test set.

This classifier was incorporated into the morphological processing method for automatic hepatocyte nuclei recognition to improve the recognition accuracy.

### 3.4.6 U-Net

A deep learning method based on U-Net was implemented as an alternative method to automatically recognize hepatocyte nuclei. Deep learning has been successfully applied to semantic segmentation in previous research [48]. Here we offer a summary of the historical development of semantic segmentation using deep learning. Many deep learning methods have been proposed. One of the basic model architectures is the convolutional neural network (CNN). Long et al. [49] modified CNN and proposed fully convolutional networks for pixel-wise labeling. Shortly after, other networks (encoder-decoder segmentation) such as SegNet [50] and U-Net [51] were proposed in 2015. In the following year, V-Net, a similar variation of U-Net, was proposed by Milletari et al. [52]. In 2017, Jégou et al. [53] adapted the U-Net-like encoder-decoder skeleton and developed Densenet. In 2018, Yu et al. [54] applied U-shaped architectures to reduce computational complexity. Several modified versions of the encode-decoder network

have been applied to semantic segmentation. DeepLabV3 [55] has output many state-of-the-art segmentation networks.

U-Net plays an important role in semantic image segmentation. In recent research, U-Net was applied and demonstrated to better result in segmentation performances on CT, MR, and ultrasound images. Brügger et al. [56] redesigned the U-Net architecture to make the network more memory efficient for 3D medical image segmentation. By adapting U-Net, Zhou et al. [57] proposed a rewiring method and applied the method on nuclei segmentation in the microscopy of CT scans. In this thesis, we used U-Net architecture [51], proposed by Olaf Ronneberger, Philipp Fischer, and Thomas Brox in 2015. U-Net does not require many training images, which was the main reason it was utilized in this research. In this thesis, the U-Net architecture was implemented as an alternative method for automatic nuclei recognition so that we can verify the accuracy of structure function curves by comparing the curves acquired from different nucleus recognition methods.

The U-Net model was trained and tested on a data set consisting of 47 ROIs whose nuclei were manually recognized. From each ROI ( $1800 \times 1800$  pixels), 64 patches for U-Net ( $256 \times 256$  pixels) were chosen. As a result, there are  $64 \times 47 = 3008$  patches for U-Net training and test in total. The test set consisted of 1004 out of 3008 and the remaining 2004 patches were used as the training set. Google Colab was used to train the model. The outputs of the test sets were the same size as the input patches ( $256 \times 256$  pixels). Reconstruction of the histological images for U-Net to their corresponding ROIs' original size ( $1800 \times 1800$  pixels) was performed. Post-processing was performed to yield recognized nuclei: Opening and closing operations were performed with a 2-pixel radius disk as the structuring element object. Watershed operations were performed to separate connected recognized nuclei.

### 3.5 Manual Nuclei Recognition

Manual recognition of hepatocyte nuclei was performed to evaluate the accuracy of the automatic recognition algorithms. A semi-automatic manual recognition program was used by first drawing a box to enclose a nucleus. After that, the program automatically drew a circle to fit the nucleus boundary. The program's output was the circle center coordinates and the corresponding radius of the fitted circle. Plotting the recorded coordinates on the corresponding original figure would result in the manual recognition in Figure 13. Manual nuclei recognition was performed in 47 ROIs.

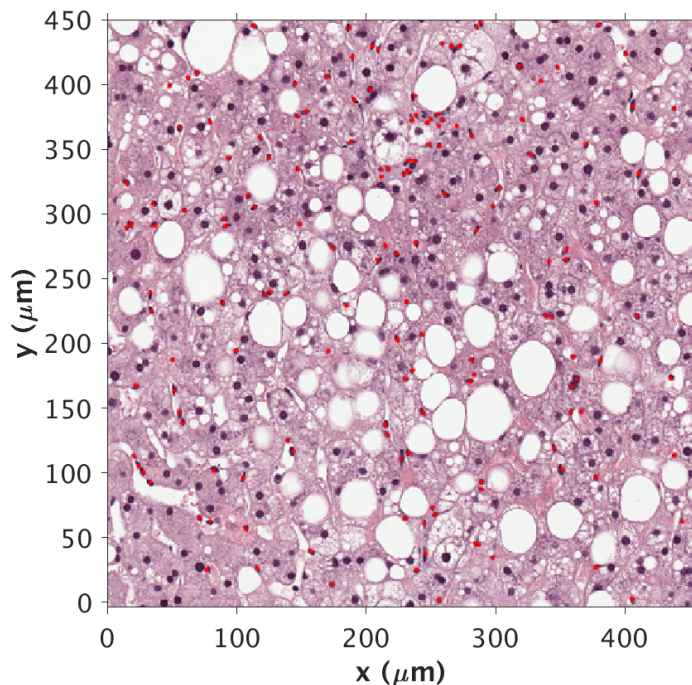


Figure 13: Manually recognized hepatocyte nuclei marked in red.

### 3.6 Structure Function Calculation from ROI

The SF was calculated by using the 2-D version of equation (4) based on the coordinates of the nuclear centers. For manual nucleus recognition, the nucleus center locations were directly recorded by the program during the manual annotation process. For automatic nucleus recognition, the nucleus center locations were calculated by using the Matlab function ‘bwconncomp’ from the binary images generated as the output of the automatic recognition algorithm (e.g., Figure 3 (i)). The scattering vector  $\mathbf{K}$  was determined as  $\mathbf{K} = \frac{2\pi}{L}(n_x\hat{x} + n_y\hat{y})$ , where  $n_x, n_y = \pm 1, \pm 2, \dots$ , and  $L$  is the side length of the ROI. The magnitude of  $\mathbf{K}$  was then determined by  $k = \frac{2\pi}{L}\sqrt{n_x^2 + n_y^2}$ . Circular averaging was performed with a resolution of  $\frac{2\pi}{L}$  for  $k$ , which means  $k$  values in a ring centered at the origin point with a width of  $\frac{2\pi}{L}$  were calculated. For backscattering, the frequency was determined by  $f = kc/4\pi$ , where the speed of sound  $c = 1540$  m/s. The frequency range used to calculate the SF was 3.4 to 40 MHz. The low-frequency limit was determined by the ROI size [18], [25] and the upper frequency was extended beyond conventional clinical frequency ranges to provide theoretical insights.

### **3.7 Evaluation of Automatic Nucleus Recognition**

This section describes how we evaluated the methods of automatic nucleus recognition and structure function curves.

#### **3.7.1 U-Net Performance of automatic nucleus recognition methods**

The manual recognition was used as the ground truth to evaluate the automatic hepatocyte nuclei recognition methods. The precision, recall, and F1 scores for evaluating the performance of the automatic recognition were computed as follows:

$$\text{Precision} = \text{True Positive} / (\text{True Positive} + \text{False Positive})$$

$$\text{Recall} = \text{True Positive} / (\text{True Positive} + \text{False Negative})$$

$$F1 = 2 \times \text{Precision} \times \text{Recall} / (\text{Precision} + \text{Recall})$$

A nucleus is considered a true positive if its automatically recognized center is within 5 pixels ( $1.3 \mu\text{m}$ ) from the center of the manually recognized nucleus. Five pixels are approximately half of the radius of a typical hepatocyte nucleus. When an automatically recognized nucleus matches multiple manually recognized nuclei, the closest match was chosen as a true positive. False positive occurs when the algorithm falsely recognized an object as a nucleus. A false negative occurs when the automatic algorithm fails to recognize an object found by manual recognition.

### 3.7.2 Evaluation by Comparing the Structure Function Curves

The SF versus frequency curves calculated based on the automatic and manual recognition were compared. The agreement of both curves was evaluated by the coefficient of determination defined as

$$R^2 = 1 - \frac{SS_{res}}{SS_{tot}}, \quad (6)$$

where  $SS_{tot}$  is the total sum of squares of the difference between structure function values from manual recognition and its mean value, and  $SS_{res}$  is the sum of squares of residuals between structure function values from manual recognition and structure function values from automatic recognition. A higher  $R^2$  indicates better agreement.

### 3.8 Comparison of the Structure Function of ROIs with Different Fat Fractions

The structure function curves were used to display the difference of ROIs with different fat fractions. We visualized how the structure function can differentiate participants with different fat fractions. The 258 ROIs consists three groups by histologically-determined fat fraction: low fat (between 0 % to 5%), moderate fat (between 5% to 15%), and high fat ( $> 15\%$ ). Note that low-fat ROIs exist for NAFLD participants due to the spatial heterogeneity in hepatic fat distribution. Out of all 258 ROIs, 78 were in the low-fat group, 104 were in the moderate-fat group, and the remaining 76 were in the high-fat group. For structure function from the

morphological processing method and the U-Net method, the average of structure function in each frequency was calculated for each group separately.

## Chapter 4: RESULTS AND DISCUSSION

### 4.1 Fat Fraction Result

Figure 14 is an example of the fat droplets recognition result of the ROIs. Figure 17 shows recognized fat fraction droplets.

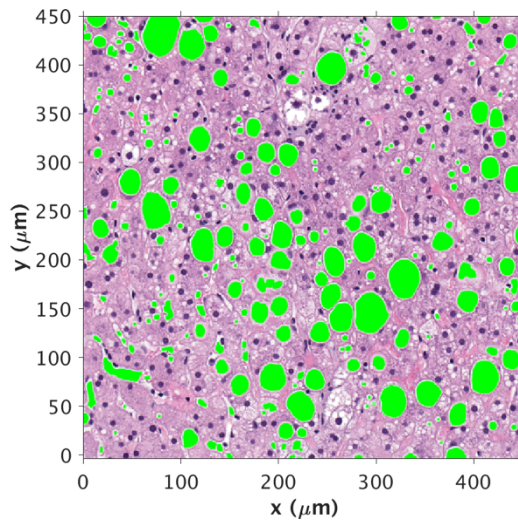


Figure 14: Example of the resulting recognition of fat droplets from one of the ROIs. The recognized fat droplets are colored in green in an ROI.

Figure 15 is a comparison of the average histologically-determined fat fraction in one to five ROIs and the MRI-PDFF for 48 participants that have MRI-PDFF data. The Pearson correlation coefficient ( $r$ -value) between the histologically-determined fat fraction and MRI-PDFF is  $0.68$  ( $p < 10^{-7}$ ), indicating a positive linear relationship between MRI-PDFF and histologically-determined per-ROI fat fraction. MRI-PDFF represents the whole liver right lobe for each participant while histologically-determined per-ROI fat fraction specifically shows the fat content in an ROI and how the fat droplets affect the distribution of hepatocytes nuclei. The

histologically-determined per-ROI fat fraction is used to compare with the SF because both were obtained from the same ROI.

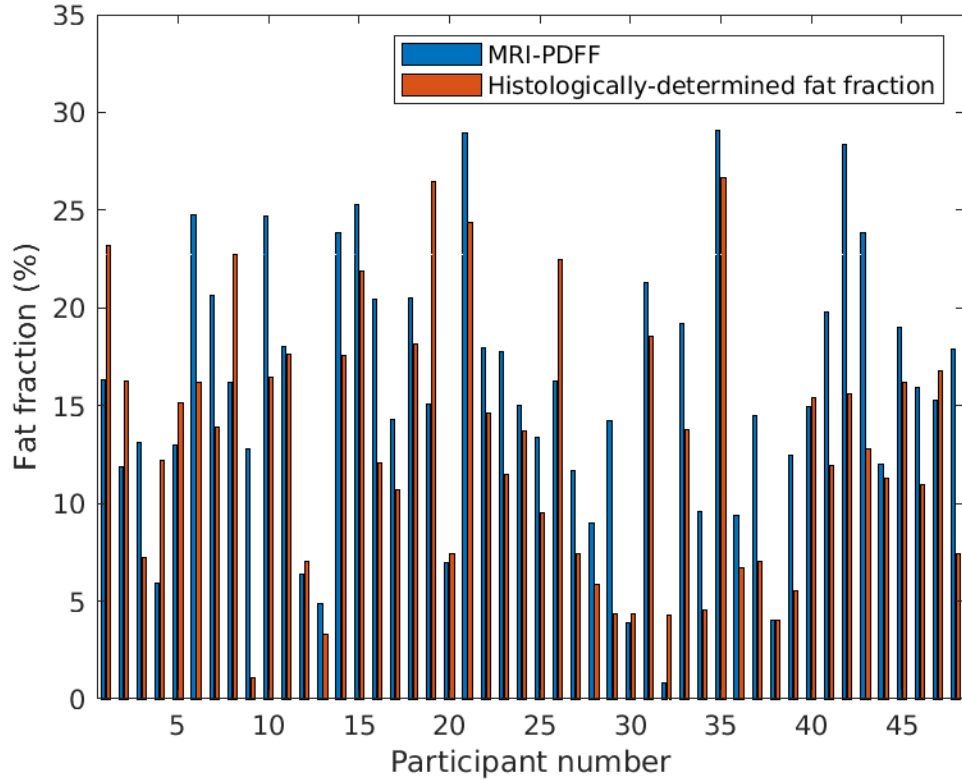


Figure 15: Comparison of the average fat fraction in 1 to 5 ROIs (orange) and the MRI-PDFF for 48 participants (blue). The horizontal axis is an unordered sequence of the participant numbers. Another 8 participants' MRI-PDFF values were unavailable and hence not shown in this figure.

## 4.2 Automatic Nuclei Recognition Result

The F1 scores of both automatic nuclei recognition methods were plotted in Figure 16 for the 47 ROIs for which manual nuclei recognition was available. In 12 out of 47 ROIs, the F1 score of the morphological processing method is higher than the U-Net method. Figure 17 is the sorted F1 score from the morphological processing method and the U-Net method. It shows that after

sorting, the F1 score from U-Net is in general higher than the F1 score from the morphological processing method. Additionally, the Pearson correlation coefficient was applied to evaluate the correlation between the fat fraction and the F1 score of the automatic nuclei recognition for both methods. For the morphological processing method, the F1 score was negatively correlated with the fat fraction ( $r = -0.3$  and  $p = 0.03$ ), indicating that the higher fat fraction can negatively affect the method's accuracy in recognizing hepatocyte nuclei. In contrast, the negative correlation between F1 score and fat fraction was less significant for the U-Net method ( $r = -0.22$  and  $p = 0.13$ ).

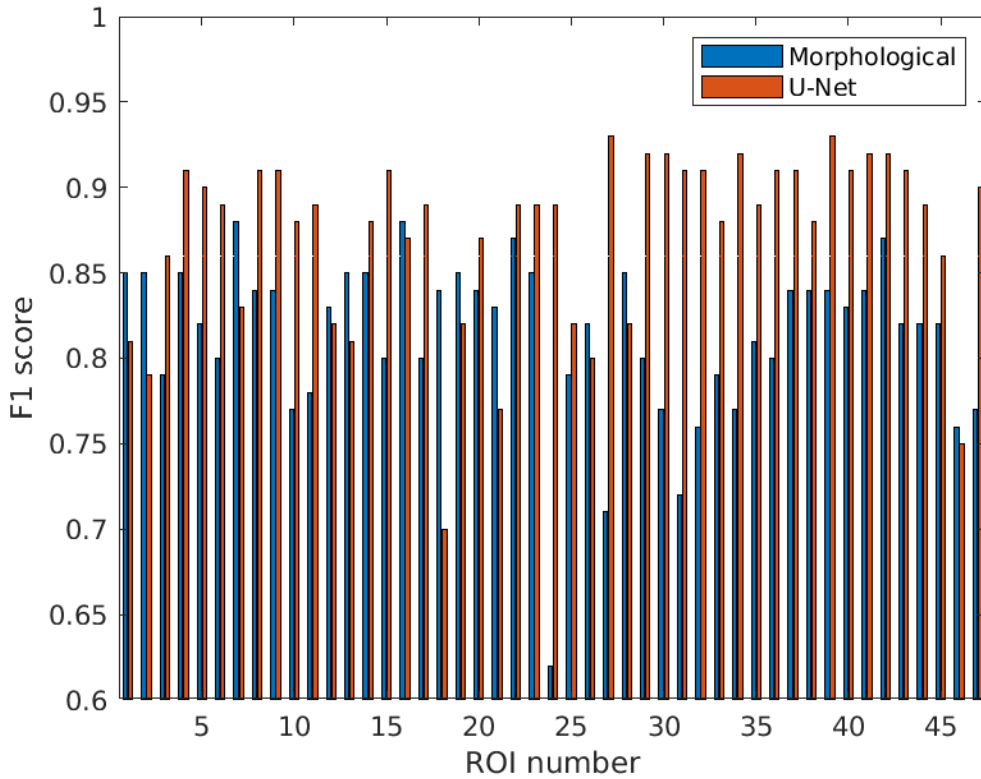


Figure 16: Plot of the F1 score 47 ROIs from 22 participants. The horizontal axis is the ROI order based on the F1 score. The blue bar represents the F1 score from the morphological processing method and the red bar represents the F1 score from the U-Net method. The blue and red bars at the same participant number represent the same participant.

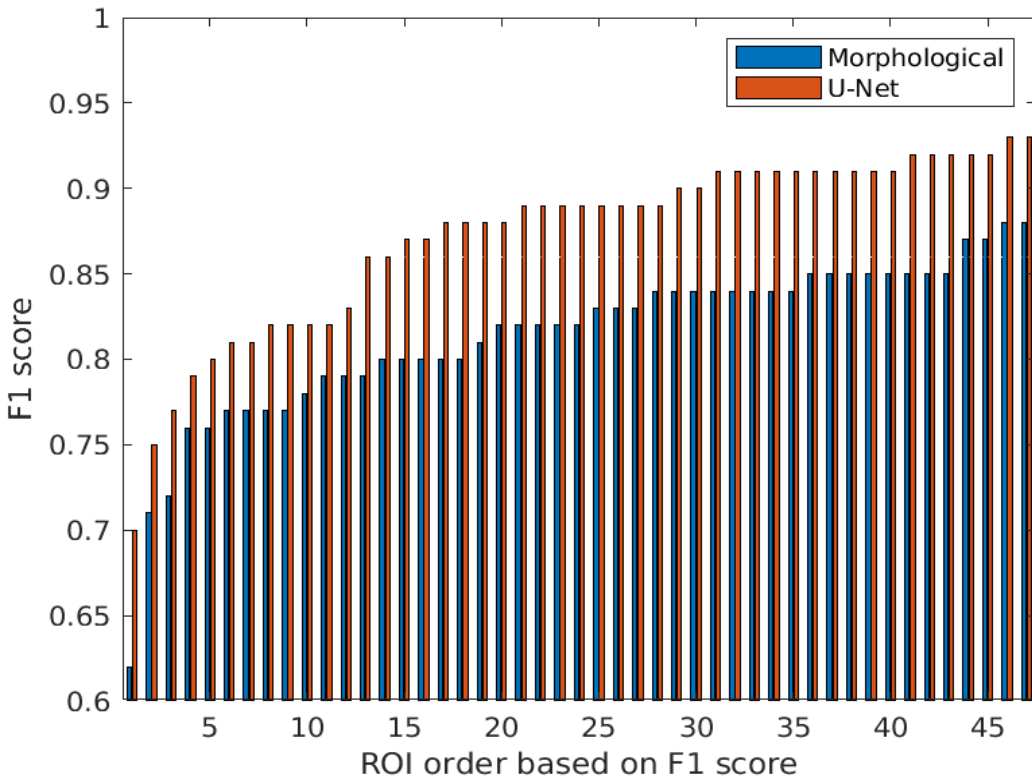


Figure 17: Comparison of the sorted F1 score calculated from the morphological processing method and U-Net method for 47 ROIs from 22 participants. The blue and red bars at the same participant number represent different participants.

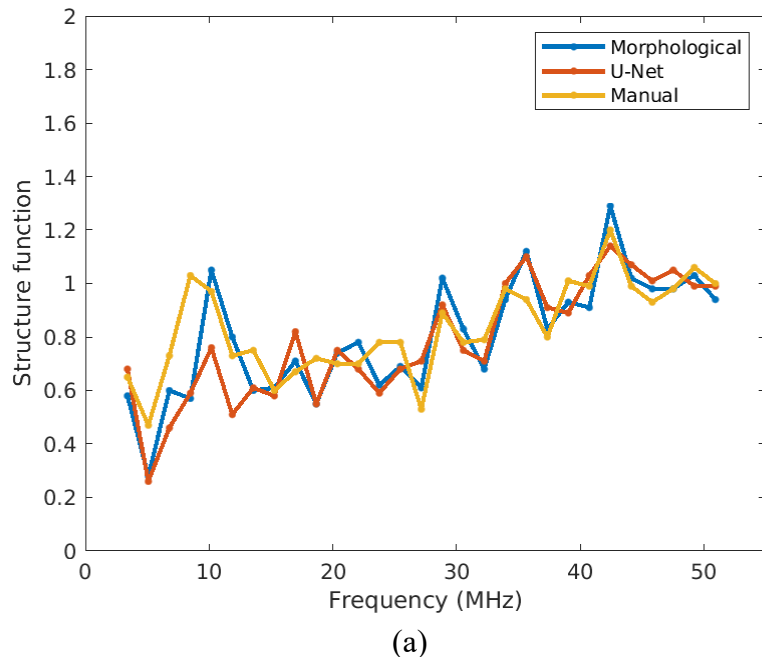
The average F1 score of 47 ROIs is 0.81 from the morphological processing method and 0.87 from the U-Net method. Both methods achieved an average F1 score greater than 80% and the results from both were applied to the following structure function analysis.

The accuracy of the morphological processing method was negatively affected by large fat fractions, possibly because more fat droplets create more edges. It is hard for the morphological processing method to distinguish some fat droplet edges and the hepatocytes nuclei. In contrast to the morphological processing method, the U-Net method does not suffer inaccuracy from the presence of fat droplets. From this standpoint, the U-Net method could be more reliable than the morphological processing method in recognizing hepatocyte nuclei.

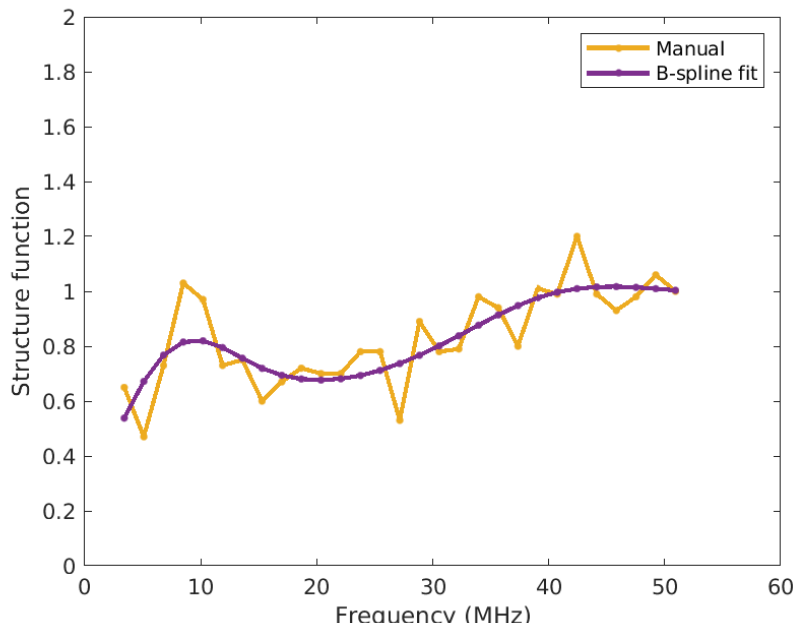
### **4.3 Structure Function Result**

Example structure function curves are plotted in Figure 18. The structure function curves were calculated from the same ROI, using automatically recognized nuclei obtained from the morphological processing method, automatically recognized nuclei obtained from the U-Net method, and manually recognized nuclei. The three structure function curves in Figure 18 (a) show similar trends. The  $R^2$  value is 0.77 between the curves denoted as ‘Morphological’ and ‘Manual’, and 0.88 between the curve denoted as ‘U-Net’ and ‘Manual’ in Figure 18 (a). These results support the use of automatic nuclei recognition of both methods for structure function calculation.

Out of the 258 ROIs, 47 ROIs have three corresponding structure function curves obtained from the manual, the morphological processing, and the U-Net method. The remaining ROIs have two corresponding structure function curves obtained from the morphological processing and the U-Net method.



(a)



(b)

Figure 18 (a): Comparison between structure function versus frequency curves obtained from automatically recognized nuclei using the morphological processing method, the U-Net method, and manually recognized nuclei method for the same ROI. (b): An example of B-spline fit to structure function curve from manually recognized nuclei method.

Figure 18 (a) evaluates the structure function curve of the U-Net method and morphological processing method. The structure function curve calculated from manual recognition was treated as the “ground truth.” The  $R^2$  value is 0.77 between the morphological processing method and ground truth, and 0.88 between the U-Net method and ground truth. These  $R^2$  values justify the use of automatic nuclei recognition of both methods for structure function calculation. The difference between  $R^2$  values indicates that the U-Net method is closer to the curve of ground truth.

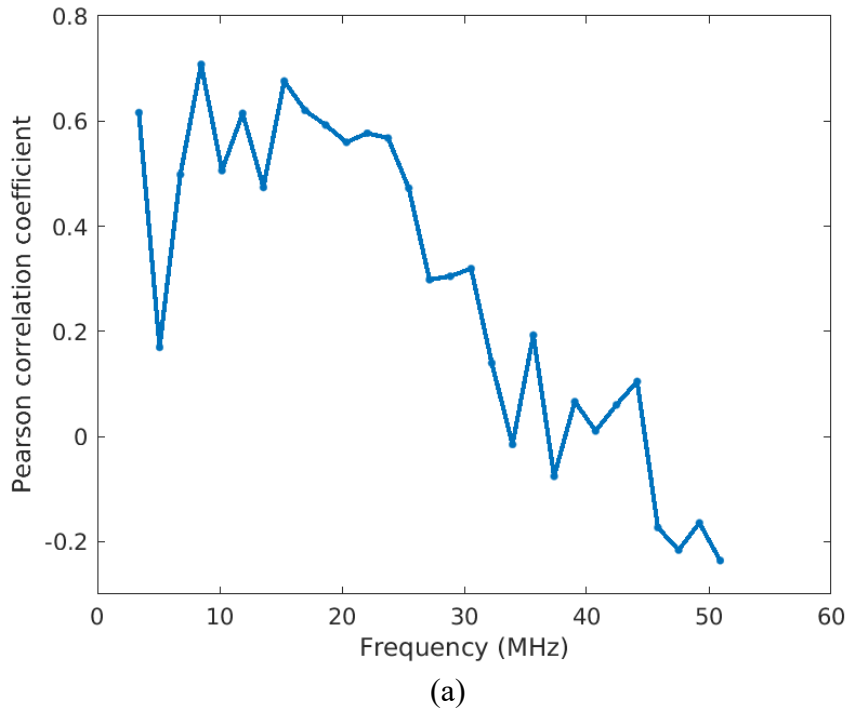
Figure 18 (b) is an example of applying B-spline fit [9] to structure function curve from manually recognized nuclei method. The B-spline fit with 6 degrees of freedom was used to smooth structure function curves of all 47 ROIs whose nuclei have been manually recognized to reduce the effect of noise in the structure function curves.

#### 4.4 Correlation between Structure Function and Fat Fraction

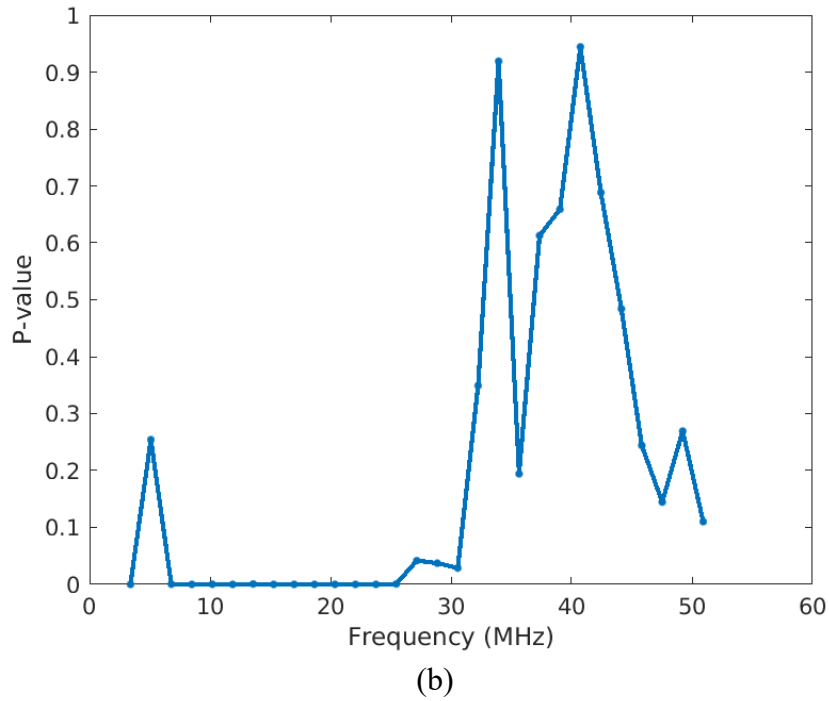
This section presents Pearson coefficient analysis of fat fraction and structure function. The structure function was calculated based on the recognized nuclei center positions from three methods: the manual recognition method, the morphological processing method, and the U-Net method.

#### **4.5.1 Correlation between Structure Function and Fat Fraction by Manual Recognition**

The Pearson correlation coefficient between fat fraction and structure function of each frequency is plotted in Figure 19. The r-value fluctuates around 0.45 and the corresponding p-value is less than 0.01 in the frequency range from 3 MHz to 25 MHz except at a frequency of 5.1 MHz. The p-value increases sharply from 25 to 30 MHz and then drops to 0 at 30 MHz. After that it increases again and keeps a high value ( $> 0.1$ ), indicating no strong evidence for the correlation between structure function and the fat fraction in the frequency range from 30 MHz to 50 MHz. When frequency = 5.1 MHz, Pearson correlation coefficient drops sharply to 0.15. This drop was possibly caused by the structure function being noisy. To demonstrate this possibility, B-spline fit was applied to smooth the SF curves. Pearson correlation coefficients are shown in Figure 20 after the B-spline fit smoothing, resulting in Pearson correlation coefficient values ranging from 0.6 to 0.86 in the frequency range from 3 MHz to 30 MHz. P-value also decreases sharply to  $10^{-10}$ . The frequency of 5.1 MHz is not an outlier anymore.



(a)



(b)

Figure 19: (a) Pearson correlation coefficient between fat fraction and SF at each frequency within 3.4 – 50 MHz calculated from 47 ROIs. The nuclei in these ROIs have been recognized manually from 14 participants with NAFLD. (b) Corresponding p-values of the Pearson correlation analysis in (a).

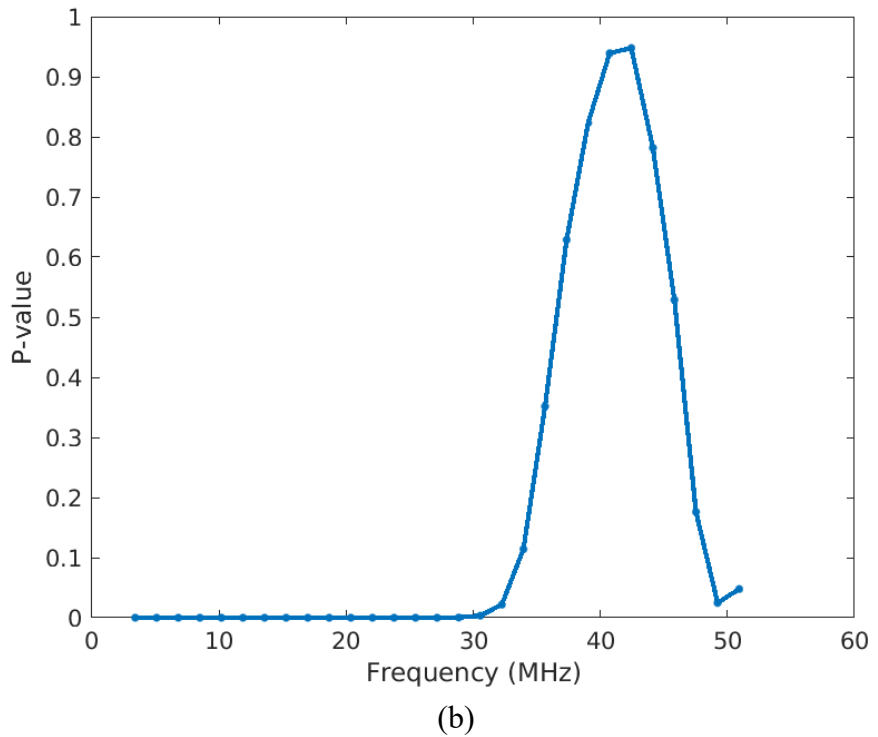
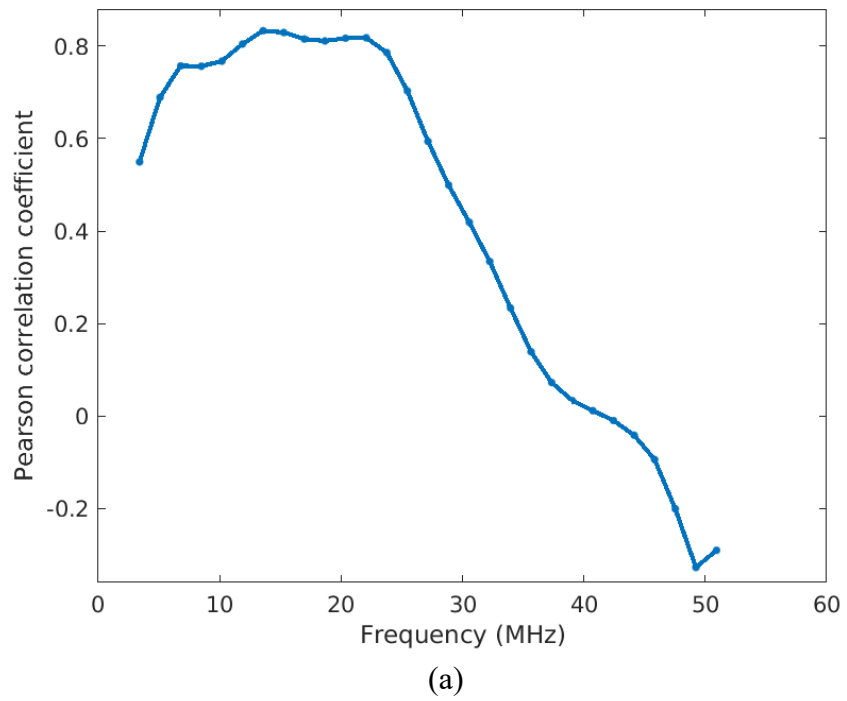
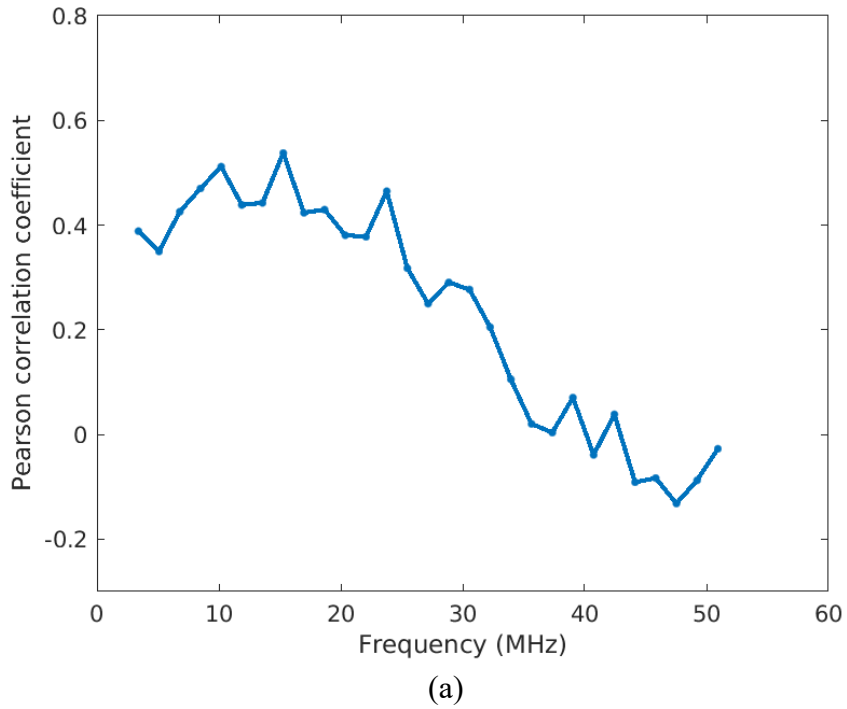


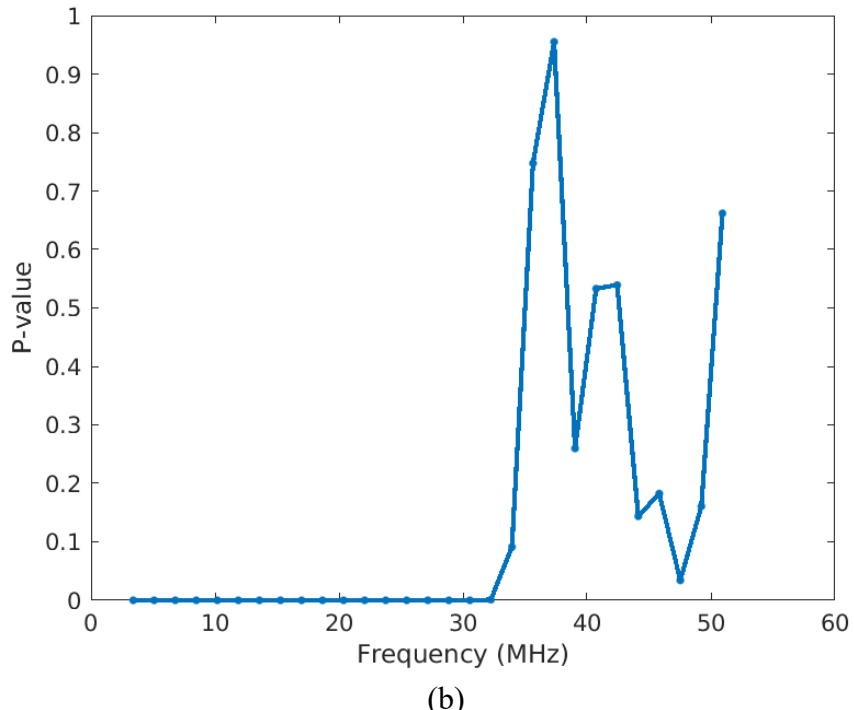
Figure 20: (a) Pearson correlation coefficient between fat fraction and SF after B-spline fit (order = 6) at each frequency within 3.4 – 50 MHz calculated from 47 ROIs. The nuclei in these ROIs have been recognized manually from 14 participants with NAFLD. (b) Corresponding p-values of the Pearson correlation analysis in (a).

## **4.5.2 Correlation between Structure Function and Fat Fraction by Morphological Processing Method**

Pearson correlation analysis was applied where the structure function was calculated from the recognized nuclei position by the morphological processing method. In Figure 21 (a), the r-value fluctuates around 0.45 at the frequency range from 6.8 MHz to 25 MHz. When frequency equals 3.4 MHz, the correlation value equals 0.40. When the frequency equals 5.1 MHz, the correlation drops to 0.35 but rises in the following frequencies up to 20 MHz. P-values, as shown in figure 24 (b), are low ( $< 10^{-4}$ ) under 31 MHz but rise sharply in the frequency range of 31 MHz to 51 MHz. In Figure 22 (a), r-value are shown after the B-spline fit smoothing, resulting in r-value values ranging from 0.4 to 0.78 in the frequency range from 3 MHz to 30 MHz. Figure 22 (b) shows a similar trend to Figure 21 (b) that p-value are low ( $< 10^{-4}$ ) under 31 MHz but rise sharply in the frequency range of 31 MHz to 51 MHz.

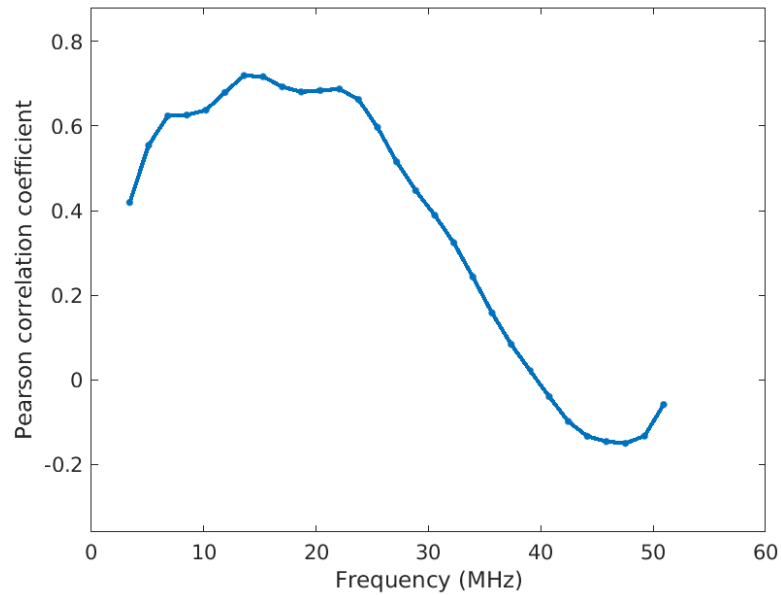


(a)

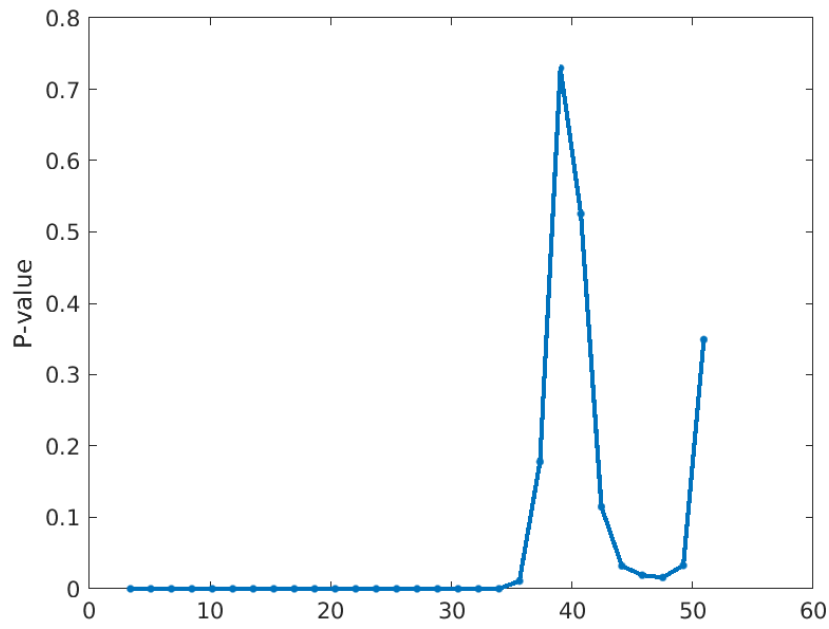


(b)

Figure 21: (a) Pearson correlation coefficient between fat fraction and SF at each frequency within 3.4 – 51 MHz calculated from 258 ROIs. The nuclei in these ROIs have been automatically recognized by morphological processing method. (b) Corresponding p-values of the Pearson correlation analysis in (a).



(a)

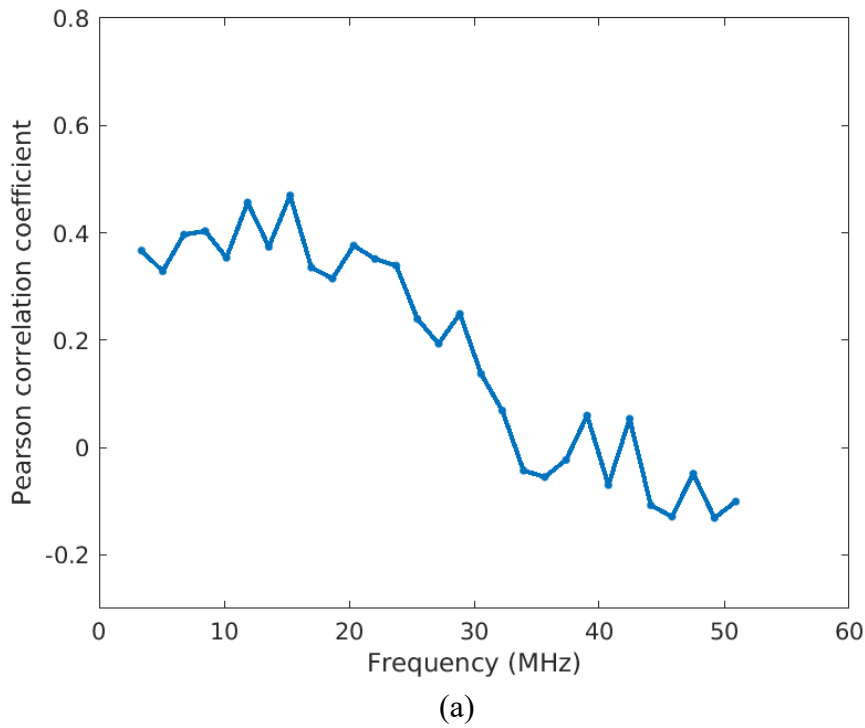


(b)

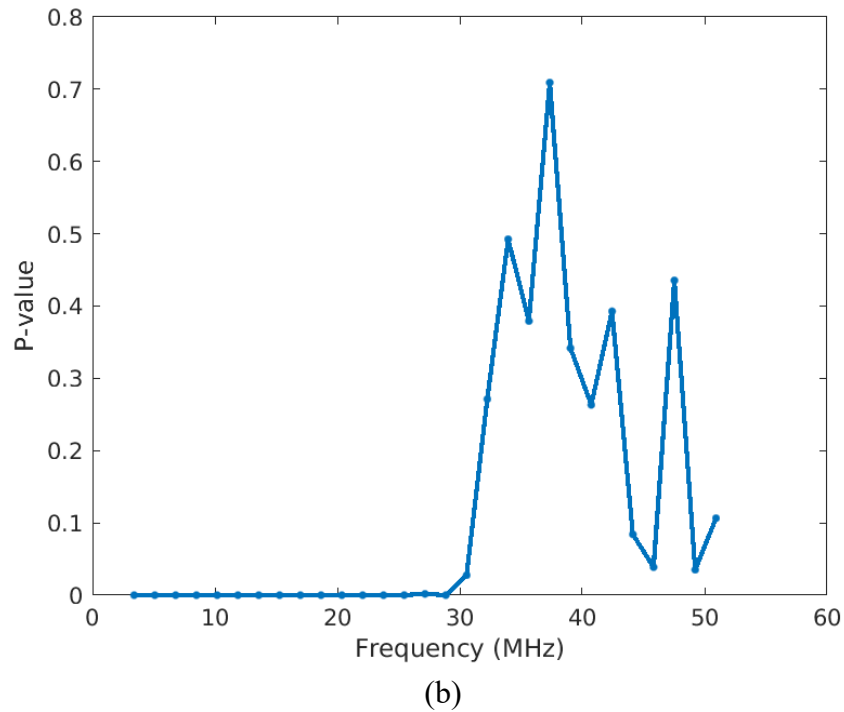
Figure 22: (a) Pearson correlation coefficient between fat fraction and SF after B-spline fit (order = 6) at each frequency within 3.4 – 50 MHz calculated from 258 ROIs. The nuclei in these ROIs have been automatically recognized by morphological processing method. (b) Corresponding p-values of the Pearson correlation analysis in (a).

#### **4.5.3 Correlation between Structure Function and Fat Fraction by U-Net**

Pearson correlation analysis was applied where the structure function was calculated from the recognized nuclei position by the U-Net method as shown in Figure 23 and Figure 24. The overall trend is similar to Figure 21 – 22. In Figure 23, The r-value fluctuates around 0.40 at the frequency range from 3.4 MHz to 20 MHz. The p-value is less than  $10^{-4}$  until the frequency reaches 29 MHz. Figure 24 (a) shows r-value after the B-spline fit smoothing, resulting in r-value values ranging from 0.39 to 0.75 in the frequency range from 3 MHz to 31 MHz. Figure 24 (b) shows a similar trend to Figure 23 (b) that p-value are low ( $< 10^{-4}$ ) under 31 MHz but rise sharply in the frequency range of 31 MHz to 51 MHz.

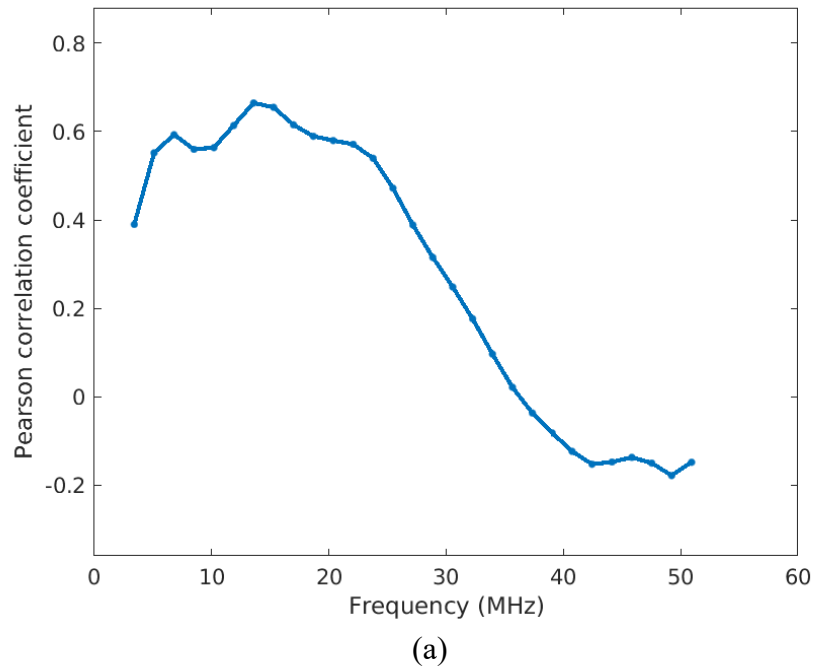


(a)

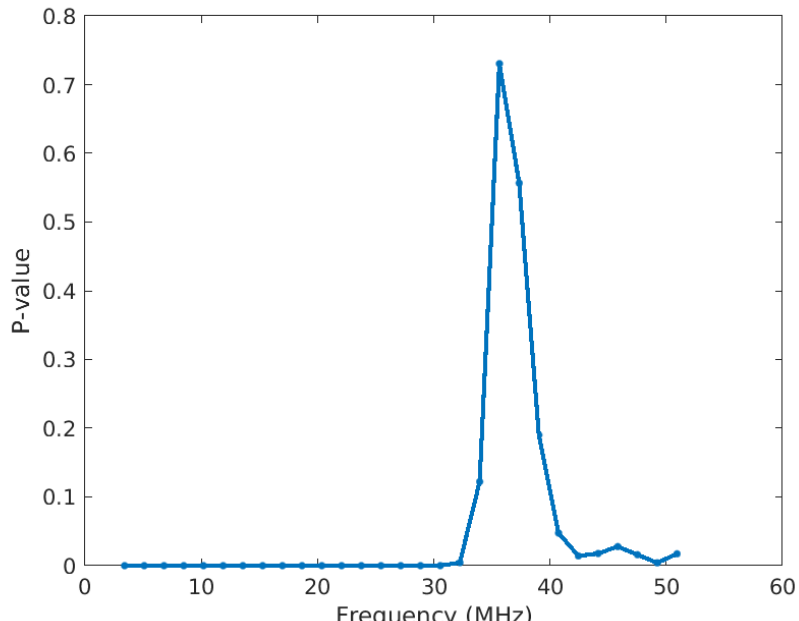


(b)

Figure 23: (a) Pearson correlation coefficient between fat fraction and SF at each frequency within 3.4 – 51 MHz calculated from 258 ROIs. The nuclei in these ROIs have been automatically recognized by the U-Net method. (b) Corresponding p-values of the Pearson correlation analysis in (a).



(a)



(b)

Figure 24: (a) Pearson correlation coefficient between fat fraction and SF after B-spline fit (order = 6) at each frequency within 3.4 – 50 MHz calculated from 258 ROIs. The nuclei in these ROIs have been automatically recognized by the U-Net method. (b) Corresponding p-values of the Pearson correlation analysis in (a).

#### **4.5.4 Summary of Pearson Correlation**

Figures 19 – 24 show similar overall trends of both r-value and p-value in Pearson correlation analysis. When the frequency is less than 20 MHz, the p-value from the manual recognition method is low enough to suggest the strong correlations between fat fraction and structure function. All three methods yielded similar results with some minor differences in details. The similarity of the results represents the rigor of this research and provides strong support that there is a positive correlation between structure function and fat fraction in the frequency range of 3.4 MHz to 25 MHz.

#### **4.6 Comparison of the Structure Function**

Average structure function curves were plotted to visualize the difference from groups of low fat, moderate fat, and high fat. The structure function curves in Figures 25 – 27 were obtained from nuclei recognition results by the morphological processing method, the U-Net method, and the manual recognition method, respectively.

Figures 25 – 27 show similar results. There are clear separations for the structure function curves of the high-fat group and low-fat group in the frequency range of 3.4 to 30 MHz. The curve of the moderate-fat group also is separated from the low-fat group.

The curves in Figure 27 are not as smooth as the curve in Figures 25 and 26 because manual recognition was available for a smaller number of ROIs.

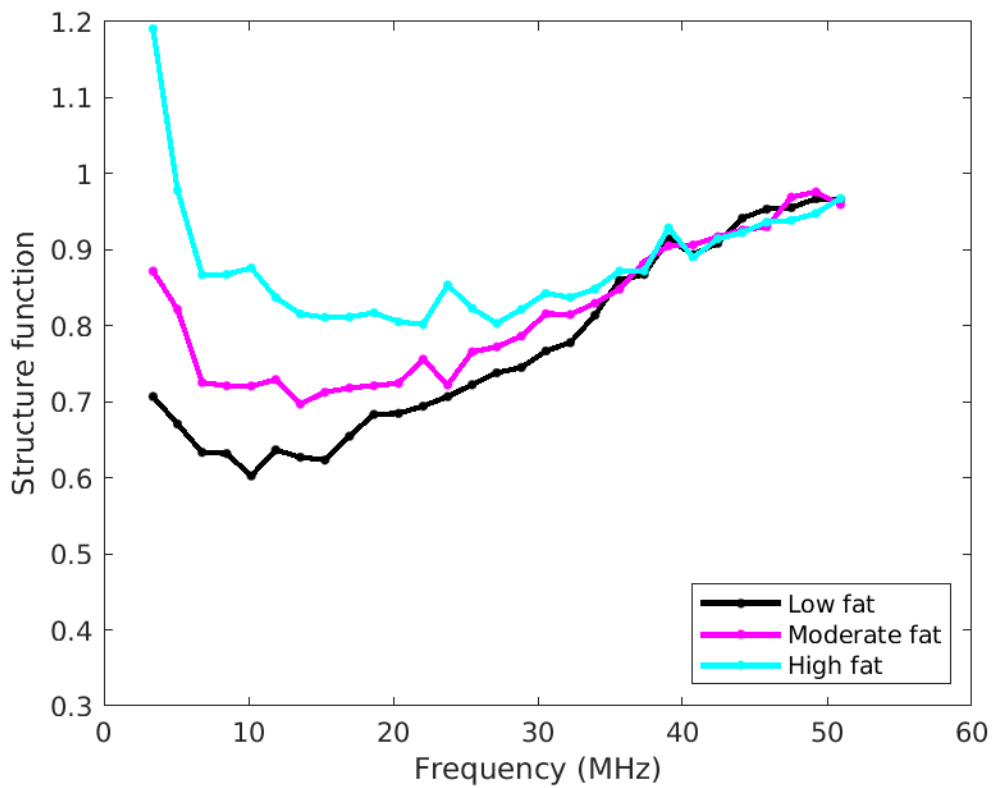


Figure 25: Average structure function curve from groups of Low fat group ( $< 5\%$ ), Moderate fat group (between  $5\%$  to  $15\%$ ), and High fat group ( $> 15\%$ ). The morphological processing method was applied to obtain the nuclei positions from which the structure function was calculated.

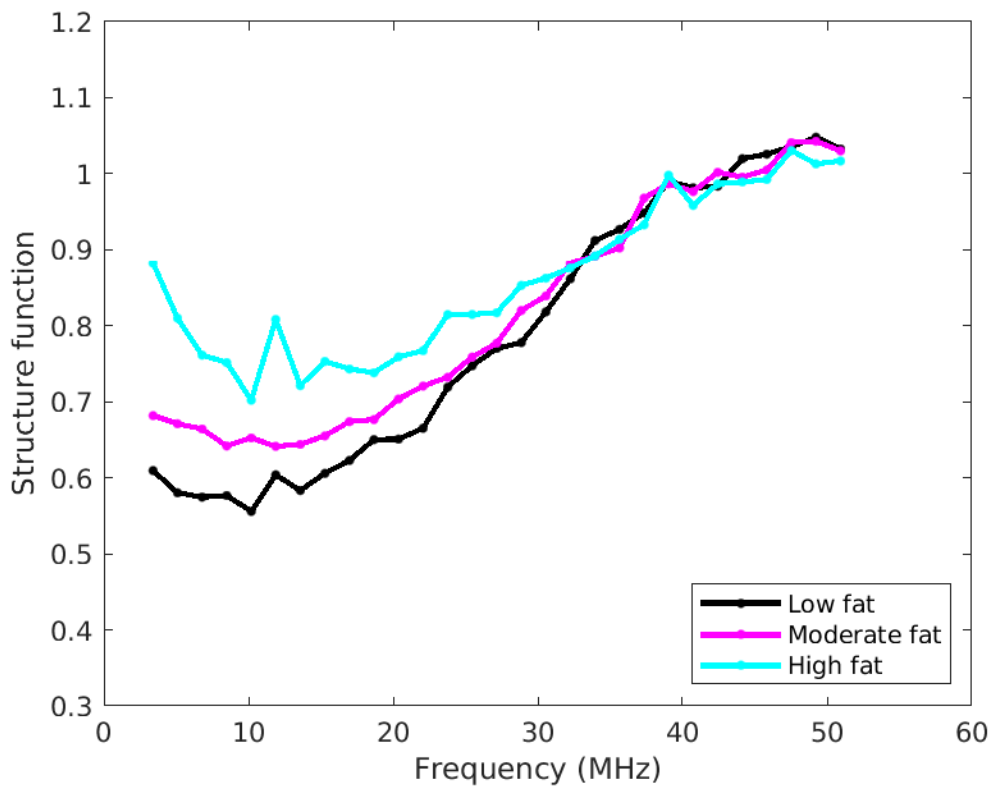


Figure 26: Average structure function curve from groups of Low fat group ( $< 5\%$ ), Moderate fat group (between  $5\%$  to  $15\%$ ), and High fat group ( $> 15\%$ ). The U-Net method was applied to obtain the nuclei positions from which the structure function was calculated.

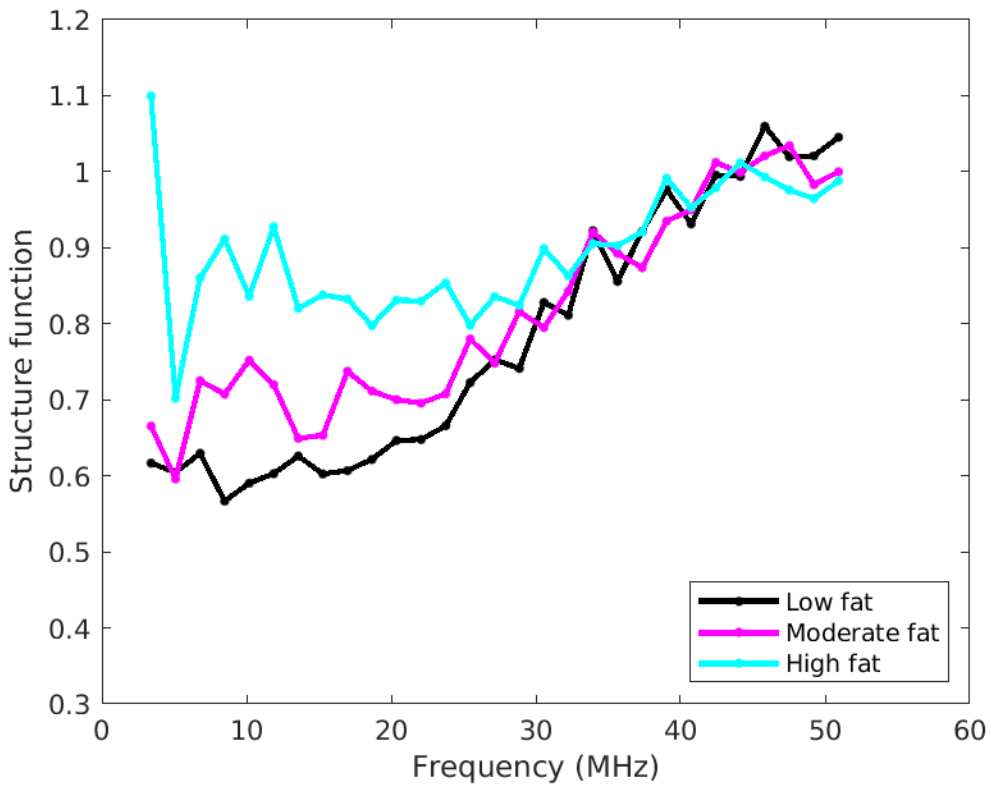


Figure 27: Average structure function curve from groups of Low fat group ( $< 5\%$ ), Moderate fat group (between  $5\%$  to  $15\%$ ), and High fat group ( $> 15\%$ ). The manual recognition method was applied to obtain the nuclei positions from which the structure function was calculated.

#### 4.7 Special NAFLD Cases

Some special NAFLD cases are worth discussing. For example, the sizes of nuclei in Figure 28 (a) are different from the rest of the ROIs selected from the same histological slides. Size information was used in automatic recognition and the size difference in Figure 28 (a) may affect the accuracy of the morphological processing method. Figures 28 (a) and (b) are in the same slide from a participant without NAFLD. The nuclei in Figure 28 (a) are larger because Figure 28 (a) contains accumulated glycogen, making the cells larger. Figure 28 (a) contains more

necrotic cells that shrink the hepatocytes. The abnormal hepatocyte nuclei in Figure 28 (a) create challenges for the automatic recognition method because of the disparity in nuclei size information. These challenges can decrease the accuracy of automatic hepatocyte nuclei and were discussed in Section 5.2.

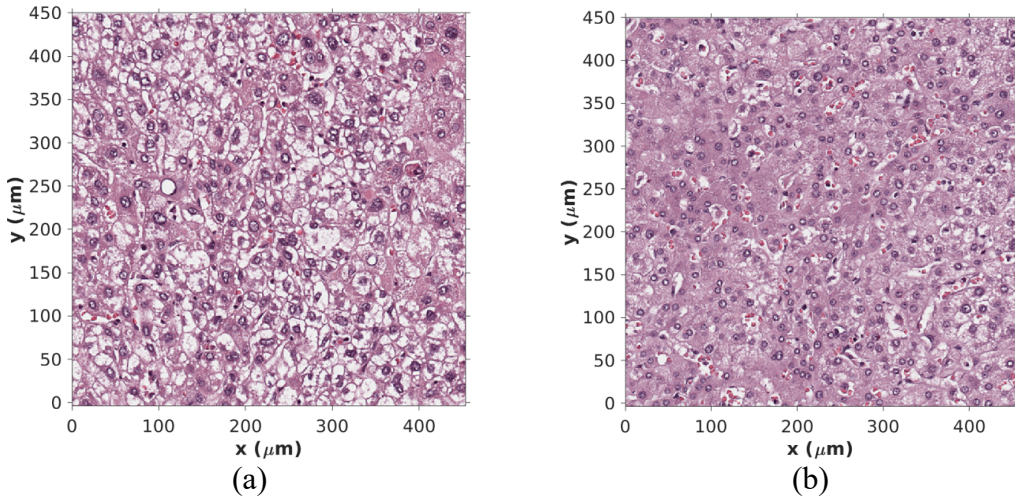


Figure 28: (a) and (b) ROIs from the same participant without NAFLD. (a) Hepatocyte nuclei with accumulated glycogen. (b) Hepatocyte nuclei in regular sizes.

#### 4.8 Discussion

The similar overall trends of both r-value and p-value in Pearson correlation analysis indicate a strong correlation between fat fraction and structure function by all three methods, morphological processing method, U-Net method, manual recognition method. We can conclude that the structure function plays an important role and cannot be neglect when modeling BSC. The positive correlation r-value is from 0.4 to 0.6 in the frequency range of 3.4 MHz to 25 MHz (including the clinical frequency range < 5 MHz) from the morphological processing method and

U-Net method. The positive correlation partially explains why previous research shows a positive correlation between fat fraction and BSC. Differences in the structure function from participants with and without NAFLD were visualized.

Our results have several limitations. First, the algorithmic automatic nuclei recognition was only tested on histological slides scanned by Leica. The algorithm was not applied to the slides scanned by other scanners such as Zeiss. As a result, the cross-scanner reproducibility of the automatic nuclei recognition algorithms was not tested. Second, the accuracy of the automatic recognition can be further improved by analyzing a larger data set.

## **Chapter 5: CONCLUSION AND FUTURE WORK**

### **5.1 Conclusion**

This thesis shows how liver fat droplets change hepatocyte nuclei distribution by analyzing H&E histopathological liver slides. Two different methods were developed to automatically recognize hepatocyte nuclei and calculate structure function. The two methods were used to improve the scientific rigor and support the hypothesis that the fat droplets change the spatial distribution of the hepatocyte nuclei and lead to changes in the structure function. The positive correlation between structure function and fat fraction was statistically significant, suggesting that the fat droplet deposition altered the structure function and the nuclei spatial distribution. Also, the positive correlation between fat fraction and structure function suggested the potential of developing the structure function to be an independent biomarker for liver fat quantification. The results demonstrated that the structure function is useful in understanding ultrasonic scattering in the human liver.

Overall, this thesis improves the understanding of the ultrasound scattering mechanisms, which could lead to better acoustic scattering models and more accurate diagnostics on NAFLD.

### **5.2 Future Work**

There is still room for improvement regarding how the fat droplets affect structure function and BSC. First, a more accurate nuclei recognition can be explored. This study shows that more accurate nuclei recognition would result in more accurate structure function curves. In addition,

the effect of some special cases mentioned in Section 4.7 could lower the accuracy of the current morphological processing method. With a better nuclei recognition method, more accurate structure function curves would lead to a more accurate correlation between fat fraction and structure function. Second, the nuclei recognition in the H&E histological slides scanned under different scanners can be explored, which will enlarge the dataset of the liver H&E histological slides and test cross-scanner reproducibility. Third, this thesis does not address the second hypothesis mentioned in Section 1.5 that fat droplets constitute acoustic scatterers in the liver and BSC increases with the number/concentration of fat droplets. This hypothesis will be investigated in future studies.

## REFERENCES

- [1] M. L. Oelze and J. Mamou, “Review of quantitative ultrasound: Envelope statistics and backscatter coefficient imaging and contributions to diagnostic ultrasound,” *IEEE Trans. Ultrason. Ferroelectr. Freq. Control*, vol. 63, no. 2, pp. 336–351, 2016.
- [2] A. Han and W. D. O’Brien, Jr., “Structure function for high concentration biophantoms of polydisperse scatterer sizes,” *IEEE Trans. Ultrason., Ferroelectr., Freq. Control*, vol. 62, no. 2, pp. 303–318, 2015.
- [3] E. J. Feleppa, F. L. Lizzi, D. J. Coleman, and M. M. Yaremko, “Diagnostic spectrum analysis in ophthalmology: A physical perspective,” *Ultrasound Med. Biol.*, vol. 12, pp. 623–631, 1986.
- [4] P. K. Tamirisa, M. R. Holland, J. G. Miller, and J. E. Perez, “Ultrasonic tissue characterization: Review of an approach to assess hypertrophic myocardium,” *Echocardiography*, vol. 18, pp. 593–597, 2001.
- [5] E. J. Feleppa, A. Kalisz, Sokil-Melgar, J., F. Lizzi, T. Liu, A. Rosado, M. Shao, W. Fair, Y. Wang, and M. Cookson, “Typing of prostate tissue by ultrasonic spectrum analysis,” *IEEE Trans. Ultrason. Ferroelectr. Freq. Control*, vol. 43, pp. 609–619, 1996.
- [6] M. F. Insana, “Modeling acoustic backscatter from kidney microstructure using an anisotropic correlation function,” *J. Acoust. Soc. Am.*, vol. 97, pp. 649–655, 1995.
- [7] M. L. Oelze, W. D. O’Brien, Jr., J. P. Blue, and J. F. Zachary, “Differentiation and characterization of rat mammary fibroadenomas and 4T1 mouse carcinomas using quantitative ultrasound imaging,” *IEEE Trans. Med. Imaging*, vol. 23, pp. 764–771, 2004.
- [8] A. Han, R. Abuhababsah, R. J. Miller, S. Sarwate, and W. D. O’Brien, Jr., “The measurement of ultrasound backscattering from cell pellet biophantoms and tumors *ex vivo*,” *J. Acoust. Soc. Amer.*, vol. 134, no. 1, pp. 686–693, 2013.
- [9] R. Sampias, G. Rolls, “H7E Staining overview: A Guide to best practices [Online],” Available: <https://www.leicabiosystems.com/knowledge-pathway/he-staining-overview-a-guide-to-best-practices/>, 2021.
- [10] S. C. Lin, E. Heba, T. Wolfson, B. Ang, A. Gamst, A. Han, J. W. Erdman, Jr., W. D. O’Brien, Jr., M. P. Andre, C. B. Sirlin, and R. Loomba, “Noninvasive diagnosis of nonalcoholic fatty liver disease and quantification of liver fat using a new quantitative ultrasound technique,” *Clin. Gastroenterol. Hepatol.*, vol. 13, no. 7, pp. 1337–1345, 2015.
- [11] J. S. Paige, G. S. Bernstein, E. Heba, E. A. C. Costa, M. Fereirra, T. Wolfson, A. C. Gamst, M. A. Valasek, G. Y. Lin, A. Han, J. W. Erdman, Jr., W. D. O’Brien, Jr., M. P. Andre, R. Loomba, and C. B. Sirlin, “A pilot comparative study of quantitative ultrasound, conventional ultrasound, and MRI for predicting histology-determined steatosis grade in adult nonalcoholic fatty liver disease,” *Am. J. Roentgenol.*, vol. 208, no. 5, pp. W168–W177, 2017.

- [12] A. Han, Y. N. Zhang, A. S. Boehringer, V. Montes, M. P. Andre, J. W. Erdman, Jr., R. Loomba, M. A. Valasek, C. B. Sirlin, and W. D. O'Brien, Jr., "Assessment of hepatic steatosis in nonalcoholic fatty liver disease using quantitative ultrasound," *Radiology*, vol. 295, no. 1, pp. 106–113, 2020.
- [13] R. Loomba and A. J. Sanyal, "The global NAFLD epidemic," *Nat Rev Gastroenterol Hepatol*, vol. 10, no. 10, pp. 686–690, 2013.
- [14] S. L. Friedman, B. A. Neuschwander-Tetri, M. Rinella, A. J. Sanyal, "Mechanisms of NAFLD development and therapeutic strategies," *Nat Med*, vol. 24, no. 7, pp. 908–922, 2018.
- [15] A. Wieckowska, A. E. Feldstein, "Diagnosis of nonalcoholic fatty liver disease: Invasive versus noninvasive," *Semin Liver Dis.*, vol. 28: pp. 386–395, 2018.
- [16] P. Angulo, "Nonalcoholic fatty liver disease," *N Engl J Med*, vol. 346, pp. 1221–1231, 2002.
- [17] E. M. Petaja, Y. Zhou, M. Havana, A. Hakkarainen, N. Lundbom, J. Ihlainen, H. Yki-Jarvinen, "Phosphorylated IGFBP-1 as a non-invasive predictor of liver fat in NAFLD," *Sci. Rep.*, vol. 6, pp. 24740, 2016.
- [18] A. C. Luchies and M. L. Oelze, "Effects of the container on structure function with impedance map analysis of dense scattering media," *J. Acoust. Soc. Amer.*, vol. 143, no. 4, pp. 2172–2181, 2018.
- [19] P. Mofrad, M. J. Contos, M. Haque, C. Sargeant, R. A. Fisher, V. A. Luketic, R. K. Sterling, M. L. Shiffman, R. T. Stravitz, A. J. Sanyal, "Clinical and histologic spectrum of nonalcoholic fatty liver disease associated with normal ALT values," *Hepatology*, vol. 37, pp. 1286–1292, 2003.
- [20] M. V. Machado, H. Cortez-Pinto, "Non-invasive diagnosis of non-alcoholic fatty liver disease. A critical appraisal," *J. Hepatol*, vol. 58: pp. 1007–1019, 2013.
- [21] C. C. Park, P. Nguyen, C. Hernandez, R. Bettencourt, K. Ramirez, L. Fortney, J. Hooker, E. Sy, M. T. Savides, M. H. Alquiraish, M. A. Valasek, E. Rizo, L. Richards, D. Brenner, C. B. Sirlin, R. Loomba, "Magnetic resonance elastography vs transient elastography in detection of fibrosis and noninvasive measurement of steatosis in patients with biopsy-proven nonalcoholic fatty liver disease," *Gastroenterology*, vol. 152, pp. 598–607, 2017.
- [22] S. B. Reeder, I. Cruite, G. Hamilton, C. B. Sirlin, "Quantitative assessment of liver fat with magnetic resonance imaging and spectroscopy," *J Magn Reson Imaging*, vol. 34, pp. 729–749, 2011.
- [23] N. S. Artz, C. D. Hines, S. T. Brunner, R. M. Agni, J. P. Kühn, A. Roldan-Alzate, G. H. Chen, S. B. Reeder, "Quantification of hepatic steatosis with dual-energy computed tomography:

comparison with tissue reference standards and quantitative magnetic resonance imaging in the ob/ob mouse," *Invest Radiol*, vol. 47, pp. 603–610, 2012.

[24] S. C. Lin, E. Heba, T. Wolfson, B. Ang, A. Gamst, A. Han, J. W. Erdman, Jr., W. D. O'Brien, Jr., M. P. Andre, C. B. Sirlin, R. Loomba, "Noninvasive diagnosis of nonalcoholic fatty liver disease and quantification of liver fat using a new quantitative ultrasound technique," *Clin Gastroenterol Hepatol*, vol. 13, pp. 1337–1345, 2015.

[25] A. Han, "A Method for Stereological Determination of the Structure Function From Histological Sections of Isotropic Scattering Media," in *IEEE Transactions on Ultrasonics, Ferroelectrics, and Frequency Control*, vol. 65, no. 6, pp. 1007-1016, June 2018.

[26] F. L. Lizzi, M. Ostromogilsky, E. J. Feleppa, M. C. Rorke, and M. M. Yaremko, "Relationship of ultrasonic spectral parameters to features of tissue microstructure," *IEEE Trans. Ultrason. Ferroelectr. Freq. Control* 33, 319–329 ~1986.

[27] D. Nicholas, "Evaluation of backscattering coefficients for excised human tissues: Results, interpretation, and associated measurements," *Ultrasound Med. Biol.* 8, 17–28 ~1982.

[28] J. C. Bamber, "Theoretical modeling of the acoustic scattering structure of human liver," *Acoust. Lett.*, vol. 3, no. 6, pp. 114–119, 1979.

[29] V. C. Anderson, "Sound scattering from a fluid sphere," *J. Acoust. Soc. Am.*, vol. 22, no. 4, pp. 426–431, 1950.

[30] M. F. Insana, R. F. Wagner, D. G. Brown, and T. J. Hall, "Describing small-scale structure in random media using pulse-echo ultrasound," *J. Acoust. Soc. Amer.*, vol. 87, no. 1, pp. 179–192, 1990.

[31] D. K. Nassiri and C. R. Hill, "The use of angular scattering measurements to estimate structural parameters of human and animal tissues," *J. Acoust. Soc. Am.* 79, 2048–2054 ~1986.

[32] A. Han, R. Abuhababsah, J. P. Blue, Jr., S. Sarwate, and W. D. O'Brien, Jr., "Ultrasonic backscatter coefficient quantitative estimates from high-concentration Chinese hamster ovary cell pellet biophantoms," *J. Acoust. Soc. Am.*, vol. 130, no. 6, pp. 4139–4147, 2011.

[33] E. Franceschini and R. Guillermin, "Experimental assessment of four ultrasound scattering models for characterizing concentrated tissuemimicking phantoms," *J. Acoust. Soc. Amer.*, vol. 132, no. 6, pp. 3735–3747, 2012.

[34] R. M. Vlad, R. K. Saha, N. M. Alaje, S. Ranieri, G. J. Czarnota, and M. C. Kolios, "An increase in cellular size variance contributes to the increase in ultrasound backscatter during cell death," *Ultrasound Med. Biol.*, vol. 36, no. 9, pp. 1546–1558, 2010.

- [35] V. Twersky, “Low-frequency scattering by correlated distributions of randomly oriented particles,” *J. Acoust. Soc. Amer.*, vol. 81, no. 5, pp. 1609–1618, 1987.
- [36] V. Twersky, “Low-frequency scattering by mixtures of correlated nonspherical particles,” *J. Acoust. Soc. Amer.*, vol. 84, no. 1, pp. 409–415, 1988.
- [37] R. K. Saha and M. C. Kolios, “Effects of cell spatial organization and size distribution on ultrasound backscattering,” *IEEE Trans. Ultrason. Ferroelectr. Freq. Control*, vol. 58, no. 10, pp. 2118–2131, 2011.
- [38] D. Savéry and G. Cloutier, “A point process approach to assessing the frequency dependence of ultrasound backscattering by aggregating red blood cells,” *J. Acoust. Soc. Amer.*, vol. 110, no. 6, pp. 3252–3262, 2001.
- [39] E. Franceschini, R. K. Saha, and G. Cloutier, “Comparison of three scattering models for ultrasound blood characterization,” *IEEE Trans. Ultrason. Ferroelectr. Freq. Control*, vol. 60, no. 11, pp. 2321–2334, 2013.
- [40] A. Han and W. D. O’Brien, Jr., “Structure function estimated from histological tissue sections,” *IEEE Trans. Ultrason., Ferroelect., Freq. Control*, vol. 63, no. 9, pp. 1296–1305, 2016.
- [41] A. Luchies, “Using Two-dimensional Impedance Maps to Study Acoustic Properties of Tissue Microstructure,” Ph.D. Thesis, University of Illinois at Urbana-Champaign, 2016.
- [42] A. Han. “Ultrasonic Characterization of Cell Pellet Biophantoms and Tumors using Quantitative Ultrasound Models,” Ph.D. Thesis, University of Illinois at Urbana-Champaign, 2014.
- [43] D. Wittekind, “Traditional staining for routine diagnostic pathology including the role of tannic acid 1 Value and limitations of the hematoxylin-eosin stain”, *Biotechnic & Histochemistry*, vol. 78, no. 5, pp. 261270, 2003.
- [44] M. Macenko *et al.*, “A method for normalizing histology slides for quantitative analysis,” 2009 IEEE International Symposium on Biomedical Imaging: From Nano to Macro, Boston, MA, pp. 1107–1110, 2009.
- [45] S. B. Reeder, H. H. Hu, C. B. Sirlin, “Proton density fat-fraction: a standardized MR-based biomarker of tissue fat concentration,” *Journal of magnetic resonance imaging: JMRI*, vol. 36, no. 5, pp. 1011–1014, 2012.
- [46] L. Najman and M. Schmitt, “Watershed of a continuous function,” In *Signal Processing (Special issue on Mathematical Morphology.)*, Vol. 38, pp. 99–112, 1994.
- [47] R. Haralick, K. Shanmugam, and I. Dinstein, “Textural Features for Image Classification,” *IEEE Trans. on Systems, Man and Cybernetics*, vol. 3, no. 6, pp. 610–621, 1973.

- [48] S. Christoph, G. W. Daniel W, “Machine learning in cell biology – teaching computers to recognize phenotypes,” *Journal of Cell Science*, vol. 126, pp. 5529–5539, 2013.
- [49] J. Long, E. Shelhamer, T. Darrell, “Fully convolutional networks for semantic segmentation,” *Proceedings of the IEEE conference on computer vision and pattern recognition*, pp. 3431–3440, 2015.
- [50] H. Noh, S. Hong, B. Han, “Learning deconvolution network for semantic segmentation,” *Proceedings of the IEEE international conference on computer vision*, pp. 1520–1528, 2015.
- [51] O. Ronneberger, P. Fischer, T. Brox, “U-Net: convolutional networks for biomedical image segmentation,” *International conference on medical image computing and computer-assisted intervention*. Springer, pp. 234–241, 2015.
- [52] F. Milletari, N. Navab, S. A. Ahmadi, “V-Net: Fully convolutional neural networks for volumetric medical image segmentation,” *2016 fourth international conference on 3D vision*. IEEE, pp. 565–571, 2016.
- [53] S. Jégou, M. Drozdzal, D. Vazquez, A. Romero, Y. Bengio, “The one hundred layers tiramisu: Fully convolutional densenets for semantic segmentation,” *Proceedings of the IEEE conference on computer vision and pattern recognition workshops*, pp. 11–19, 2017.
- [54] C. Yu, J. Wang, C. Peng, C. Gao, G. Yu, N. Sang, “BiSeNet: Bilateral segmentation network for real-time semantic segmentation,” *Proceedings of the European conference on computer vision (ECCV)*. Springer, pp. 334–349, 2018.
- [55] L. C. Chen, Y. Zhu, G. Papandreou, F. Schroff, H. Adam, “Encoder-decoder with atrous separable convolution for semantic image segmentation,” *Proceedings of the European conference on computer vision*, pp. 801–818, 2018.
- [56] R. Brügger, C. F. Baumgartner, E. Konukoglu, “A partially reversible U-Net for memory-efficient volumetric image segmentation,” *arXiv:190606148*, 2019.
- [57] Z. Zhou, M. M. Siddiquee, N. Tajbakhsh, J. Liang, “UNet++: a nested U-Net architecture for medical image segmentation,” *Deep learning in medical image analysis and multimodal learning for clinical decision support*, Springer, pp. 3–11, 2018.